Nuclear thermodynamics from chiral low-momentum interactions

Corbinian Wellenhofer,[1] Jeremy W. Holt,[2] Norbert Kaiser,[1] and Wolfram Weise[1,3]
[1]*Physik Department, Technische Universität München, D-85747 Garching, Germany*
[2]*Department of Physics, University of Washington, Seattle, Washington 98195, USA*
[3]*ECT*, Villa Tambosi, I-38123 Villazzano (TN), Italy*
(Received 8 April 2014; published 30 June 2014)

We investigate the thermodynamic equation of state of isospin-symmetric nuclear matter with microscopic nuclear forces derived within the framework of chiral effective field theory. Two- and three-body nuclear interactions constructed at low-resolution scales form the basis for a perturbative calculation of the finite-temperature equation of state. The nuclear force models and many-body methods are benchmarked against bulk properties of isospin-symmetric nuclear matter at zero temperature, which are found to be well reproduced when chiral nuclear interactions constructed at the lowest resolution scales are employed. The calculations are then extended to finite temperatures, where we focus on the liquid-gas phase transition and the associated critical point. The Maxwell construction is applied to construct the physical equation of state, and the value of the critical temperature is determined to be $T_c = 17.2$–19.1 MeV, in good agreement with the value extracted from multifragmentation reactions of heavy ions.

DOI: 10.1103/PhysRevC.89.064009 PACS number(s): 21.65.Mn, 21.30.Fe

I. INTRODUCTION

The equation of state (EoS) of nuclear matter is of fundamental importance for heavy-ion collisions and for a range of astrophysical phenomena, including neutron star structure and evolution, nucleosynthesis, as well as the dynamics of core-collapse supernovae and binary neutron star mergers. The recent observation of two-solar-mass neutron stars [1,2] places strong constraints on the neutron matter EoS. To support neutron stars of such mass, the EoS has to be comparatively stiff, which at first glance appears to favor neutron star models with primarily nucleonic degrees of freedom and challenges models that include exotic condensates or deconfined quark matter [1,3,4]. The interpretation of expected observations of gravitational wave forms linked to binary neutron star (or neutron star—black hole) mergers provides further motivation for calculations of the dense nucleonic matter equation of state with reliable uncertainty estimates. Such astrophysical applications require a realistic EoS for neutron matter with a small admixture of protons. As a prerequisite for any such discussion, an essential condition is to have an EoS for isospin-symmetric nuclear matter that is consistent with empirical constraints provided by nuclear thermodynamics. The present work focuses on this issue.

With the development of chiral effective field theory (χEFT), high-precision two- and many-nucleon forces constrained by the symmetry breaking pattern of QCD provide the foundation for systematic studies of low-energy nuclear structure and reactions. Once the low-energy constants that parametrize unresolved short-distance nuclear dynamics are fixed by fits to few-nucleon observables (as a function of the chosen resolution scale), nuclear many-body properties result as pure predictions. Empirical properties of infinite homogeneous nuclear matter, such as the saturation point and compressibility of isospin-symmetric nuclear matter at zero temperature as well as the first-order transition from a liquid to a vapor phase at finite temperature, are then nontrivial tests of the many-body methods and nuclear force models. Particularly the critical point of the liquid-gas phase transition is essential in constraining the finite-temperature domain of the nuclear EoS. Estimates for this point have been obtained through the analysis of data from multifragmentation, fission, and compound nuclear decay experiments [5,6]. The critical temperature T_c in particular was located at approximately 18 MeV.

In recent years, various aspects of the zero-temperature nuclear EoS from χEFT have been studied in detail by numerous authors within widely different many-body frameworks [7–21]. The picture that arises is that low-momentum microscopic nuclear interactions associated with a resolution scale around 400–450 MeV facilitate the convergence of the EoS in many-body perturbation theory at and near nuclear matter saturation density ($\rho_0 \simeq 0.17$ fm^{-3}), while an accurate treatment of very low-density matter must account for nuclear clustering and nonperturbative features of the nucleon-nucleon interactions associated with the physics of large scattering lengths. The thermodynamic properties of neutron matter have been studied in Ref. [22], while in-medium chiral perturbation theory at finite temperature was used to explore isospin-asymmetric nuclear matter over a range of proton fractions and densities [23]. For an earlier study of nuclear matter at finite temperatures using phenomenological Skyrme forces, see Ref. [24]. In the present work we take the initial steps toward a complementary microscopic study of nuclear thermodynamics across the densities and isospin asymmetries relevant for astrophysical simulations of supernovae and neutron stars. We compute the thermodynamic equation of state of isospin-symmetric nuclear matter from several sets of chiral low-momentum interactions and investigate their thermodynamic consistency.

The paper is organized as follows. In Sec. II we provide details of the different two- and three-body potentials that specify the microscopic input for the subsequent calculations. In Sec. III we proceed with a discussion of many-body perturbation theory generalized to finite temperatures. The use of a temperature- and density-dependent effective

TABLE I. Parameters for the different sets of chiral low-momentum two- and three-body interactions used in this work. For the n3lo NN potentials relative momenta are restricted by a smooth regulator with cutoff scale Λ and steepness parameter n, whereas in the case of the VLK two-body potentials there is a sharp cutoff. With the cutoff scale and the regulator width taken from the respective two-body regulator the different three-body potentials are completely determined by the values of c_E, c_D, and $c_{1,3,4}$.

	Λ (fm^{-1})	n	c_E	c_D	c_1 (GeV^{-1})	c_3 (GeV^{-1})	c_4 (GeV^{-1})
n3lo500	2.5	2	–0.205	–0.20	–0.81	–3.2	5.4
n3lo450	2.3	3	–0.106	–0.24	–0.81	–3.4	3.4
n3lo414	2.1	10	–0.072	–0.4	–0.81	–3.0	3.4
VLK23	2.3	∞	–0.822	–2.785	–0.76	–4.78	3.96
VLK21	2.1	∞	–0.625	–2.062	–0.76	–4.78	3.96

two-nucleon potential [8,9,25,26] to approximate the second-order three-body contributions is discussed in detail, as well as the temperature-dependent self-energy corrections to the single-nucleon energies. In Sec. IV we examine our results for the thermodynamic EoS of isospin-symmetric nuclear matter. Finally, in Sec. V we give a summary of the main results and an outlook for future investigations of the nuclear many-body problem with the use of chiral low-momentum interactions.

II. CHIRAL LOW-MOMENTUM TWO- AND THREE-BODY INTERACTIONS

The modern theory of nuclear forces is based on chiral effective field theory [27,28], the low-energy realization of quantum chromodynamics. Its regime of applicability is governed by a separation of scales, where the hard scale is given by the chiral symmetry breaking scale $\Lambda_\chi \sim 1$ GeV, and the soft scale is associated with small nucleon momenta Q that for many phenomena of interest are of the same order of magnitude as the pion mass m_π. The Feynman diagrams contributing to interactions between nucleons are then organized in an expansion in powers of the parameter Q/Λ_χ. Short-distance dynamics associated with the length scale $1/\Lambda_\chi$ is parametrized by low-energy constants (LECs) that are generally fixed by fitting to two-nucleon scattering phase shifts and in the case of nuclear three-body forces to properties of ^{3}H and ^{3}He. The results of these fitting procedures are not unique, and there exist various sets of LECs in the literature (e.g., [28–31]), all of which lead (by construction) to consistent results in the few-body sector.

Because of the limited energy regime accessible to χEFT, chiral nuclear interactions are typically regulated at a scale Λ lying between the low- and high-energy regimes: $Q < \Lambda < \Lambda_\chi$. Regarding two-body forces, a common way to enforce such a restriction is to multiply the nucleon-nucleon potential $V_{\rm NN}$ with a smooth regulator function of the form,

$$f(p,p') = \exp[-(p/\Lambda)^{2n} - (p'/\Lambda)^{2n}], \qquad (1)$$

where p and p' are the absolute values of the relative momenta of the two nucleons before and after the collision.[1] In the following, we employ two-nucleon potentials constructed at the resolution scales $\Lambda = 414, 450, 500$ MeV (see Refs. [12,19,32,33] for additional details). In each case, we employ as well the respective next-to-next-to-leading order (N2LO) chiral three-body interaction (depending on the parameters c_E, c_D, and $c_{1,3,4}$). The implementation of consistent N3LO chiral many-nucleon forces remains a challenge in contemporary nuclear structure theory, but progress toward this end is being achieved [10]. We hereafter denote these three sets of chiral two- and three-body potentials by n3lo414, n3lo450, and n3lo500. Because of the different regulating functions used in the respective potentials, different values of LECs emerge from fits to few-body observables. The resulting values for the five LECs that appear in the leading-order three-body diagrams are given in the first three rows of Table I.

As the cutoff scale is reduced below 500 MeV in the construction of chiral nuclear interactions, precision fits to nucleon-nucleon scattering phase shifts deteriorate [34,35]. An alternative scheme for obtaining low-momentum nuclear interactions is to employ renormalization group (RG) techniques [34,36] that by construction leave low-energy observables invariant. In the case of an evolution of the NN potential based on half-on-shell K-matrix equivalence the resulting potential is usually denoted by $V_{\text{low-}k}(\Lambda)$, with Λ being a sharp cutoff in momentum space [37]. For cutoffs in the range $\Lambda \simeq 2.1$ fm^{-1}, the RG evolved potential is universal, i.e., independent of the input potential. This method has the advantage of producing low-momentum NN potentials directly through the evolution of partial-wave matrix elements, however, the inclusion of induced many-nucleon forces is crucial. In view of this, Nogga *et al.* [38] have used the leading-order 3N forces with the values of the $c_{1,3,4}$ constants equal to the ones extracted by the Nijmegen group in an analysis of NN scattering data [31] and determined c_E and c_D by fitting to the binding energies of ^{3}H, ^{3}He, and ^{4}He. The resulting LECs for two different $V_{\text{low-}k}$ potentials (both constructed by evolving the n3lo500 NN potential) can be found in the last two rows of Table I.

To summarize, we will analyze nuclear thermodynamics through five different sets of two- and three-body potentials. These can be used to probe a variety of aspects associated with the choice of resolution scale and low-energy constants. Of particular interest will be the comparison of nuclear potentials defined at the same resolution scale but constructed via RG methods or by refitting LECs.

[1] To be precise, p (and similarly p') is defined as half of the relative momentum of the two nucleons, i.e., $p = |\vec{k}_1 - \vec{k}_2|/2$.

III. MANY-BODY PERTURBATION THEORY FOR NUCLEAR MATTER

With the use of low-momentum interactions, many-body perturbation theory (MBPT) becomes applicable for the investigation of the nuclear many-body system [39]. In the present section we recall the main aspects of this framework, and give analytical expressions for the different terms contributing to the free energy density, both in the case of zero as well as finite temperatures. We begin by summarizing the main results for a free Fermi gas. The interacting many-nucleon system is then introduced and we present the general perturbation series for the energy density (zero temperature) and the grand canonical potential density (finite temperature), and discuss the relationship between both series, which motivates the Kohn-Luttinger-Ward formalism. Explicit expressions for the different contributions at first and second order in MBPT are then given in terms of partial-wave amplitudes. Following this, we compute the temperature- and density-dependent effective NN potential from the leading-order chiral three-nucleon force. We then examine the anomalous contributions which arise in the case of finite temperatures, and finally we calculate the temperature-dependent self-energy corrections to the single-nucleon energies.

A. Free Fermi gas

Although the free Fermi gas can easily be treated fully relativistically, we give here the expressions for the energy density and grand canonical potential density for a nonrelativistic Fermi gas and include relativistic effects by a correction term. The single-particle energies are given by the formula $\varepsilon_p = p^2/2M$.

Zero temperature. The particle density of the system in the ground state depends only on the Fermi momentum k_F, which signifies the highest occupied energy level. The density is given by

$$\rho(k_F) = \frac{2k_F^3}{3\pi^2}. \tag{2}$$

This expression is exact both for a relativistic and a nonrelativistic Fermi gas. The energy per particle, including the first relativistic correction, is given by

$$\bar{E}_0(k_F) = \frac{3k_F^2}{10M} - \frac{3k_F^4}{56M^3}. \tag{3}$$

Finite temperatures. The grand canonical potential density (with the relativistic correction constructed in Ref. [40]) is given by

$$\Omega_0(\mu_0,T) = -\frac{2}{3\pi^2}\int_0^\infty dp\,\frac{p^4}{M} n_p - \frac{1}{4\pi^2}\int_0^\infty dp\,\frac{p^6}{M^3} n_p, \tag{4}$$

where μ_0 is the (nonrelativistic) chemical potential, $\beta = 1/T$ is the inverse temperature, and $n_p = 1/[1+\exp(\beta(\varepsilon_p - \mu_0))]$ is the Fermi-Dirac distribution function. The particle density then follows from a standard thermodynamic relation, i.e.,

$$\begin{aligned}\rho(\mu_0,T) &= -\frac{\partial\Omega_0}{\partial\mu_0} = \frac{2}{\pi^2}\int_0^\infty dp\, p^2\, n_p \\ &= -\sqrt{2}\left(\frac{M}{\beta\pi}\right)^{\frac{3}{2}} \mathrm{Li}_{3/2}(-\exp(\beta\mu_0)),\end{aligned} \tag{5}$$

where $\mathrm{Li}_\nu(x) = \sum_{k=1}^\infty k^{-\nu}x^k$ is the polylogarithmic function of index ν. Because for the free Fermi gas the pressure isotherms $P_0(\mu_0) = -\Omega_0(\mu_0)$ are strictly convex, the above relation is invertible with respect to $\mu_0(\rho,T)$. For densities $\rho < -\sqrt{2}\,[M/(\beta\pi)]^{3/2}\,\mathrm{Li}_{3/2}(-1) \simeq 0.000\,727\,(T/\mathrm{MeV})^{3/2}\,\mathrm{fm}^{-3}$ the chemical potential is negative, and its behavior in the limit of vanishing densities is given by

$$\mu_0(\rho,T) \xrightarrow{\rho\to 0} \frac{1}{\beta}\ln\left(\frac{\rho}{\sqrt{2}}\left(\frac{\beta\pi}{M}\right)^{\frac{3}{2}}\right), \tag{6}$$

which, using $\mathrm{Li}_\nu(x) \xrightarrow{x\to 0} x$, follows from inverting Eq. (5) in the limit $\mu_0 \to -\infty$.

From Eqs. (4) and (5) one can calculate the free energy density, $F_0(\mu_0,T) = \mu_0\rho(\mu_0,T) + \Omega_0(\mu_0,T)$, which reproduces the energy density $E_0(k_F) = \rho(k_F)\bar{E}_0(k_F)$ in the zero-temperature limit:

$$F_0(\mu_0,T) \xrightarrow{T\to 0} E_0(k_F)\,\Big|_{\rho\ \text{fixed}}, \quad \text{where} \quad \mu_0 \xrightarrow{T\to 0} \frac{k_F^2}{2M}\,\Big|_{\rho\ \text{fixed}}. \tag{7}$$

B. Many-body perturbation series: General discussion

Zero temperature. The energy density $E = \langle\Psi_0|\mathcal{H}|\Psi_0\rangle\,/\,\langle\Psi_0|\Psi_0\rangle$ of the interacting many-nucleon system with Hamiltonian $\mathcal{H} = \mathcal{H}_0 + \lambda\mathcal{V}$ is given by the following perturbation series (known as the Brueckner-Goldstone formula [41,42]):

$$E(k_F) = E_0(k_F) + \lambda E_1(k_F) + \lambda^2 E_2(k_F) + \mathcal{O}(\lambda^3), \tag{8}$$

where $|\Psi_0\rangle$ is the exact ground state of the interacting system, $\mathcal{H}_0$ is the Hamiltonian of the noninteracting system, $\mathcal{V} = \mathcal{V}_{\mathrm{NN}} + \mathcal{V}_{\mathrm{3N}}$ is the interaction part of the Hamiltonian, and λ is a counting parameter (introduced only for bookkeeping reasons). In Eq. (8), $E_0(k_F)$ corresponds to the energy density of a noninteracting nucleon gas. The different contributions contained in E_1 and E_2 are given in terms of expectation values with respect to the noninteracting ground state $|\Phi_0\rangle$, which is characterized by the occupation of all energy levels below the Fermi energy $\varepsilon_F = k_F^2/2M$ (where $M \simeq 938.9\,\mathrm{MeV}$ is the average nucleon mass). Hence, all terms in Eq. (8) are parametrized by k_F, which is related to the nucleon density via Eq. (2). From the perspective of statistical mechanics Eq. (8) therefore amounts to a calculation in the canonical ensemble, with the free energy density given by $F(\rho,T=0) = E(k_F)$.

Finite temperatures. The imaginary-time (Matsubara) formalism leads to the following perturbation series for the grand canonical potential density Ω, or the negative pressure P:

$$\begin{aligned}\Omega(\mu,T) = -P(\mu,T) &= \Omega_0(\mu,T) + \lambda\Omega_1(\mu,T) \\ &\quad + \lambda^2\Omega_2(\mu,T) + \mathcal{O}(\lambda^3).\end{aligned} \tag{9}$$

In contrast to the zero-temperature perturbation series, all terms in the above expression are functions of the chemical potential μ of the interacting system (in addition to temperature T), corresponding to the grand canonical ensemble. Moreover, compared to Eq. (8) there are additional terms (beginning at

order λ^2), the so-called *anomalous contributions*. Apart from these differences, the explicit form of the different terms in Eq. (9) is the same as in the zero-temperature case, except one has finite-temperature Fermi-Dirac distributions instead of step functions.

Kohn-Luttinger-Ward formalism. The zero-temperature limit of the thermodynamic equation of state calculated using Eq. (9) does not reproduce the equation of state obtained from the Brueckner-Goldstone formula. In the case of realistic two- and three-body forces the Brueckner-Goldstone formula is known to produce the desired van der Waals type EoS of isospin-symmetric nuclear matter. This result cannot be obtained from Eq. (9) because in the part of the liquid-gas coexistence region where the (analytical) free energy density $F(\rho,T)$ is nonconvex (with respect to ρ), the corresponding pressure isotherms (as functions of chemical potential) $P(\mu,T)$ are multivalued. It is impossible to obtain such a feature in a grand canonical calculation; or more generally, in the case of a system that is unstable with respect to phase mixing, the canonical and the grand canonical descriptions are not equivalent, and the Legendre transformation between both is not invertible [43].

For a consistent continuation of the Brueckner-Goldstone formula to finite temperatures, one should use a perturbation series for the free energy density $F(\rho,T)$, i.e., employ a calculation in the canonical ensemble. The method for constructing such a perturbation series for $F(\rho,T)$, based on the grand canonical one, Eq. (9), was introduced by Kohn and Luttinger [44] and elaborated by Luttinger and Ward [45]. This method, which was used also by other authors (e.g., [22,23,40]), works as follows. Instead of calculating $F(\rho,T)$ directly from Eq. (9) via $\rho = -\partial\Omega/\partial\mu$ and $F = \Omega + \mu\rho$, one constructs an expansion about the noninteracting system (free Fermi gas) with (formally) the same density:

$$\rho(\mu_0,T) = -\frac{\partial\Omega_0(\mu_0,T)}{\partial\mu_0} \equiv -\frac{\partial\Omega(\mu,T)}{\partial\mu} = \rho(\mu,T). \quad (10)$$

The chemical potential is then formally expanded in terms of the counting parameter, $\mu = \mu_0 + \lambda\mu_1 + \lambda^2\mu_2 + \mathcal{O}(\lambda^3)$. Expanding each term $\partial\Omega_i(\mu,T)/\partial\mu$ around μ_0 and solving Eq. (10) iteratively for increasing powers of λ gives expressions for the μ_i, $i \geqslant 1$, as functions of μ_0, e.g.,

$$\mu_1(\mu_0,T) = -\left.\frac{\partial\Omega_1/\partial\mu}{\partial^2\Omega_0/\partial\mu^2}\right|_{\mu_0}. \quad (11)$$

Finally, expanding each term $\Omega_i(\mu,T)$ in the defining relation for the free energy density, $F = \Omega + \mu\rho$, around μ_0 leads to the following expression for $F(\mu_0,T)$:

$$F(\mu_0,T) = F_0(\mu_0,T) + \lambda\Omega_1(\mu_0,T) + \lambda^2\left(\Omega_2(\mu_0,T) - \frac{1}{2}\frac{(\partial\Omega_1/\partial\mu_0)^2}{\partial^2\Omega_0/\partial\mu_0^2}\right) + \mathcal{O}(\lambda^3). \quad (12)$$

Note that all terms in this equation are evaluated at μ_0, which is in one-to-one correspondence with the nucleon density ρ as specified by Eq. (5). Moreover, it can be verified that for spherically symmetric Fermi surfaces and rotationally invariant as well as isospin-symmetric interactions the additional derivative term at order λ^2, which is hereafter referred to as the second-order *anomalous derivative term* (ADT), cancels the second-order anomalous contribution in the zero-temperature limit. Therefore, the above expression for the free energy density satisfies the desired consistency relation,

$$F(\mu_0,T) \xrightarrow{T\to 0} E(k_F)\big|_{\rho\,\text{fixed}}, \quad \text{where} \quad \mu_0 \xrightarrow{T\to 0} \left.\frac{k_F^2}{2M}\right|_{\rho\,\text{fixed}}. \quad (13)$$

The EoS obtained with Eq. (12) can then of course not be the same as the one resulting from the grand canonical expression, Eq. (9). The deviations between them are from the truncation of the Taylor expansions of $\Omega(\mu,T)$ and $\partial\Omega(\mu,T)/\partial\mu$ around μ_0 at order λ^2.

C. Many-body perturbation series: contributions

We now give the explicit form of the first- and second-order contributions in the Kohn-Luttinger-Ward formula, Eq. (12). For reasons of clarity we use antisymmetrized interactions, i.e., $\tilde{V}_{\text{NN}} = \mathscr{A}_{\text{NN}} V_{\text{NN}}$ and $\tilde{V}_{\text{3N}} = \mathscr{A}_{\text{3N}} V_{\text{3N}}$, with antisymmetrization operators $\mathscr{A}_{\text{NN}} = 1 - P_{12}$ and $\mathscr{A}_{\text{3N}} = (1 - P_{12})(1 - P_{13} - P_{23})$. Up to second order in $\tilde{V}_{\text{NN}}$ and first order in $\tilde{V}_{\text{3N}}$ there are then four different contributions,[2] represented diagrammatically in Fig. 1.

Two-nucleon force. The first-order and the second-order normal contributions to the grand canonical potential density are given by

$$\Omega_{1,\text{NN}}(\mu_0,T) = \frac{1}{2}\,\text{tr}_{\sigma_1,\tau_1}\,\text{tr}_{\sigma_2,\tau_2}\int\frac{d^3k_1}{(2\pi)^3}\int\frac{d^3k_2}{(2\pi)^3}\; n_{k_1}n_{k_2} \times \langle \mathbf{12}\,|(1 - P_{12})V_{\text{NN}}|\,\mathbf{12}\rangle\,, \quad (14)$$

$$\Omega_{2,\text{normal}}(\mu_0,T) = -\frac{1}{8}\left(\prod_{i=1}^{4}\text{tr}_{\sigma_i,\tau_i}\int\frac{d^3k_i}{(2\pi)^3}\right)(2\pi)^3\,\delta(\vec{k}_1 + \vec{k}_2 - \vec{k}_3 - \vec{k}_4)\frac{n_{k_1}n_{k_2}\bar{n}_{k_3}\bar{n}_{k_4} - \bar{n}_{k_1}\bar{n}_{k_2}n_{k_3}n_{k_4}}{\varepsilon_3 + \varepsilon_4 - \varepsilon_1 - \varepsilon_2} \times |\langle \mathbf{12}\,|(1 - P_{12})V_{\text{NN}}|\,\mathbf{34}\rangle|^2\,, \quad (15)$$

where $\bar{n}_k = 1 - n_k$. The second-order anomalous contribution is given by

$$\Omega_{2,\text{anomalous}}(\mu_0,T) = -\frac{\beta}{2}\left(\prod_{i=1}^{3}\text{tr}_{\sigma_i,\tau_i}\int\frac{d^3k_i}{(2\pi)^3}\right)n_{k_1}n_{k_2}\bar{n}_{k_2}n_{k_3} \times\langle \mathbf{12}|(1 - P_{12})V_{\text{NN}}|\mathbf{12}\rangle\,\langle \mathbf{23}\,|(1 - P_{12})V_{\text{NN}}|\,\mathbf{23}\rangle\,. \quad (16)$$

Three-nucleon force. There are three different contributions to the N2LO three-nucleon force in χEFT: a three-nucleon contact diagram (proportional to the low-energy constant c_E),

[2]The second-order anomalous derivative term is not counted here; it follows immediately from Ω_0 and $\Omega_{1,\text{NN}}$.

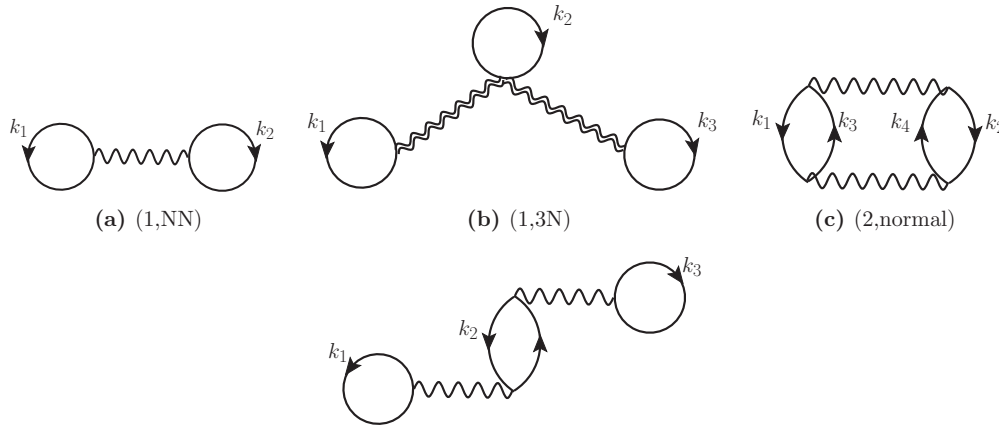

(a) (1,NN) (b) (1,3N) (c) (2,normal) (d) (2,anomalous)

FIG. 1. Antisymmetrized Goldstone diagrams representing the (a) first-order NN, (b) first-order 3N, (c) second-order normal NN, and (d) second-order anomalous NN contributions. Wavy lines represent interactions mediated by $\tilde{V}_{\rm NN}$; double-wavy lines symbolize $\tilde{V}_{\rm 3N}$.

a one-pion exchange diagram (proportional to c_D), and a two-pion exchange diagram (with low-energy constants c_1, c_3, and c_4). The first-order many-body contribution arising from these diagrams can be written in the compact form,

$$\Omega_{1,3\rm N}(\mu_0,T) = \int_0^\infty dk_1\,\frac{k_1}{2\pi^2}\int_0^\infty dk_2\,\frac{k_2}{2\pi^2}\int_0^\infty dk_3 \times \frac{k_3}{2\pi^2}\mathcal{K}_3\, n_{k_1} n_{k_2} n_{k_3}, \tag{17}$$

where $\mathcal{K}_3 = \mathcal{K}_3^{(c_E)} + \mathcal{K}_3^{(c_D)} + \mathcal{K}_3^{(\rm Hartree)} + \mathcal{K}_3^{(\rm Fock)}$. The many-body diagrams associated with these four different kernels $\mathcal{K}_3^{(i)}$ are depicted in Fig. 2.

When used in combination with low-momentum two-nucleon interactions, the three-body potential is usually multiplied with a smooth regulator in terms of Jacobi momenta P and Q [9]. Concerning the first-order 3N contributions we have found the effect of this regulator to be negligible over the range of considered densities and temperatures. Leaving out the regulator, the kernels can be simplified to the following expressions (where $g_A \simeq 1.29$ is the axial-vector strength, $f_\pi \simeq 92.4\,\rm MeV$ is the pion decay constant, $\Lambda_\chi \simeq 700\,\rm MeV$, and $m_\pi \simeq 138\,\rm MeV$ is the average pion mass):

$$\mathcal{K}_3^{(c_E)} = -\frac{12 c_E}{f_\pi^4 \Lambda_\chi} k_1 k_2 k_3, \tag{18}$$

$$\mathcal{K}_3^{(c_D)} = \frac{3 g_A c_D}{f_\pi^4 \Lambda_\chi} k_3 \left(k_1 k_2 - \frac{m_\pi^2}{4}\ln\frac{m_\pi^2+(k_1+k_2)^2}{m_\pi^2+(k_1-k_2)^2}\right), \tag{19}$$

$$\mathcal{K}_3^{(\rm Hartree)} = \frac{3 g_A^2}{f_\pi^4} k_3 \left[2(c_3-c_1)m_\pi^2 \ln\frac{m_\pi^2+(k_1+k_2)^2}{m_\pi^2+(k_1-k_2)^2} - 4c_3 k_1 k_2 + (c_3-2c_1)m_\pi^4 \times \left(\frac{1}{m_\pi^2+(k_1+k_2)^2} - \frac{1}{m_\pi^2+(k_1-k_2)^2}\right)\right], \tag{20}$$

$$\mathcal{K}_3^{(\rm Fock)} = \frac{g_A^2}{f_\pi^4 k_3}\left[3c_1 m_\pi^2 H(k_1)H(k_2) + \left(\frac{c_3}{2} - c_4\right)X(k_1)X(k_2) + (c_3+c_4)Y(k_1)Y(k_2)\right]. \tag{21}$$

The functions $H(k_i)$, $X(k_i)$, and $Y(k_i)$ in the Fock contribution are

$$H(k_i) = k_i + \frac{k_3^2 - k_i^2 - m_\pi^2}{4k_3}\ln\frac{m_\pi^2+(k_i+k_3)^2}{m_\pi^2+(k_i-k_3)^2}, \tag{22}$$

$$X(k_i) = 2k_i k_3 - \frac{m_\pi^2}{2}\ln\frac{m_\pi^2+(k_i+k_3)^2}{m_\pi^2+(k_i-k_3)^2}, \tag{23}$$

$$Y(k_i) = \frac{k_i}{4k_3}\left(5k_3^2 - 3k_i^2 - 3m_\pi^2\right) + \frac{3\left(k_i^2-k_3^2+m_\pi^2\right)^2 + 4m_\pi^2 k_3^2}{16k_3^2} \times \ln\frac{m_\pi^2+(k_i+k_3)^2}{m_\pi^2+(k_i-k_3)^2}. \tag{24}$$

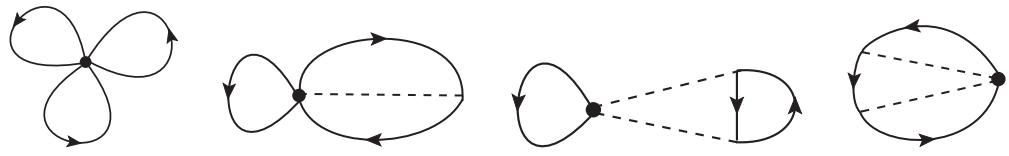

(a) c_E (b) c_D (c) Hartree (d) Fock

FIG. 2. Contributions to $\Omega_{1,3\rm N}$ from chiral 3N forces at N2LO. Dashed lines represent pions.

D. Partial-wave representation of two-body contributions

The two-nucleon interaction $\tilde{V}_{\rm NN}$ is usually given in terms of partial-wave matrix elements. In this section we give the partial-wave expanded form of the two-body contributions presented in the previous section, both for zero and for finite temperatures, as well as the expressions needed to calculate the second-order anomalous derivative term.

First-order contribution. The partial-wave expansion of the matrix elements in Eq. (14) results in the following expression:

$$\Omega_{1,\rm NN}(\mu_0,T) = \frac{2}{\pi^3}\int_0^\infty dp\, p^2 \int_0^\infty dK\, K^2 \mathcal{F}(p,K) \times \sum_{J,\ell,S}(2J+1)(2\mathcal{T}+1)\langle p|\tilde{V}_{\rm NN}^{J,\ell,\ell,S,\mathcal{T}}|p\rangle. \tag{25}$$

Here, $\tilde{V}_{\rm NN}^{J,\ell_1,\ell_2,S,\mathcal{T}}$ are the matrix elements of the antisymmetrized two-body potential with respect to total angular momentum states $|J\ell_i S\mathcal{T}\rangle$, and $\vec{K}$ is half the total momentum of the two nucleons. The function $\mathcal{F}(p,K)$ is given by

$$\mathcal{F}(p,K) = \int_{-1}^{1} d\cos\theta_K\; n_{|\vec{K}-\vec{p}|} n_{|\vec{K}+\vec{p}|} = \frac{\ln(1+e^{\eta+2x}) - \ln(e^{2x}+e^{\eta})}{x(e^{2\eta}-1)}, \tag{26}$$

where θ_K is the angle between $\vec{K}$ and $\vec{p}$, $x = \beta\frac{Kp}{2M}$, and $\eta = \beta(\frac{K^2+p^2}{2M} - \mu_0)$.

The expression for the corresponding zero-temperature contribution to the energy per nucleon $\bar{E}$ can be simplified further. It is given by

$$\bar{E}_{1,\rm NN}(k_F) = \frac{2}{\pi}\int_0^{k_F} dp\, p^2 \left(1 - \frac{3p}{2k_F} + \frac{p^3}{2k_F^3}\right) \sum_{J,\ell,S}(2J+1)(2\mathcal{T}+1)\langle p|\tilde{V}_{\rm NN}^{J,\ell,\ell,S,\mathcal{T}}|p\rangle. \tag{27}$$

Second-order normal contribution. The partial-wave representation of the second-order normal contribution is given by

$$\Omega_{2,\rm normal}(\mu_0,T) = -\frac{8}{\pi^2}M\int_0^\infty dp_1\, p_1^2 \int_{-1}^{1} d\cos\theta_1 \int_0^\infty dp_2\, p_2^2 \int_{-1}^{1} d\cos\theta_2 \int_0^\infty dK\, K^2\, \frac{\mathcal{F}(p_1,p_2,K,\theta_1,\theta_2)}{p_2^2-p_1^2} \times \sum_S \sum_{J,\ell_1,\ell_2} \sum_{J',\ell_1',\ell_2'} i^{\ell_2-\ell_1} i^{\ell_1'-\ell_2'} \langle p_1|\tilde{V}_{\rm NN}^{J,\ell_1,\ell_2,S,\mathcal{T}}|p_2\rangle\langle p_2|\tilde{V}_{\rm NN}^{J',\ell_2',\ell_1',S,\mathcal{T}}|p_1\rangle(2\mathcal{T}+1) \sum_{M,m,m'} \mathcal{C}(\theta_1,\theta_2). \tag{28}$$

The function $\mathcal{C}(\theta_1,\theta_2)$ collects spherical harmonics and Clebsch-Gordan coefficients:

$$\mathcal{C}(\theta_1,\theta_2) = \mathcal{Y}_{\ell_1,(M-m)}(\theta_1)\mathcal{Y}_{\ell_2,(M-m')}(\theta_2)\mathcal{Y}_{\ell_2',(M-m')}(\theta_2)\mathcal{Y}_{\ell_1',(M-m)}(\theta_1) \times \langle \ell_1(M-m)Sm|JM\ell_1 S\rangle\langle JM\ell_2 S|\ell_2(M-m')Sm'\rangle \times \langle \ell_2'(M-m')Sm'|J'M\ell_2' S\rangle\langle J'M\ell_1' S|\ell_1'(M-m)Sm\rangle. \tag{29}$$

Here, $\mathcal{Y}_{\ell,m}(\theta)$ denotes the spherical harmonics without the azimuthal part $e^{im\phi}$. The other function $\mathcal{F}(p_1,p_2,K,\theta_1,\theta_2)$ is given by

$$\mathcal{F}(p_1,p_2,K,\theta_1,\theta_2) = n_{|\vec{K}+\vec{p}_1|}n_{|\vec{K}-\vec{p}_1|}\bar{n}_{|\vec{K}+\vec{p}_2|}\bar{n}_{|\vec{K}-\vec{p}_2|} - \bar{n}_{|\vec{K}+\vec{p}_1|}\bar{n}_{|\vec{K}-\vec{p}_1|}n_{|\vec{K}+\vec{p}_2|}n_{|\vec{K}-\vec{p}_2|}, \tag{30}$$

where the angles $\theta_{1,2}$ are measured with respect to (half) the total momentum $\vec{K}$. Note that the integrand in Eq. (28) is nonsingular at $p_1 = p_2$.

To obtain the zero-temperature expression for the second-order normal contribution the Fermi-Dirac distributions in Eq. (30) have to be substituted with Heavyside step functions. The inequalities associated with these step functions can be absorbed into the boundaries of the integrals, which then results in the following expression:

$$\bar{E}_{2,\rm normal}(k_F) = -\frac{24}{k_F^3}M\int_0^{k_F} dK\, K^2 \int_0^{\sqrt{k_F^2-K^2}} dp_1\, p_1^2 \int_{\sqrt{k_F^2-K^2}}^\infty dp_2\, p_2^2 \int_{-\min(\alpha_1,1)}^{\min(\alpha_1,1)} d\cos\theta_1 \int_{-\min(-\alpha_2,1)}^{\min(-\alpha_2,1)} d\cos\theta_2 \frac{1}{p_2^2-p_1^2} \times \sum_S \sum_{J,\ell_1,\ell_2} \sum_{J',\ell_1',\ell_2'} i^{\ell_2-\ell_1} i^{\ell_1'-\ell_2'} \langle p_1|\tilde{V}_{\rm NN}^{J,\ell_1,\ell_2,S,\mathcal{T}}|p_2\rangle\langle p_2|\tilde{V}_{\rm NN}^{J',\ell_2',\ell_1',S,\mathcal{T}}|p_1\rangle(2\mathcal{T}+1) \sum_{M,m,m'} \mathcal{C}(\theta_1,\theta_2), \tag{31}$$

where $\alpha_i = (k_F^2 - K^2 - p_i^2)/(2Kp_i)$.

Second-order anomalous contribution. Expanding the matrix elements in Eq. (16) in terms of partial waves one arrives at

$$\Omega_{2,\rm anomalous}(\mu_0,T) = -\frac{16}{\pi^2}\beta\int_0^\infty dk\, k^2 n_k\bar{n}_k \left[\int_0^\infty dp\, p^2 \sum_{J,\ell,\ell',S} i^{\ell-\ell'}\left\langle\frac{p}{2}\middle|\tilde{V}_{\rm NN}^{J,\ell,\ell',S,\mathcal{T}}\middle|\frac{p}{2}\right\rangle \int_{-1}^{1} d\cos\theta_p\; n_{|\vec{p}+\vec{k}|} \sum_{Mm_st_z} \mathcal{C}'(\theta_p)\right]^2, \tag{32}$$

where θ_p is the angle between $\vec{p}$ and $\vec{k}$, and

$$\mathcal{C}'(\theta_p) = \mathcal{Y}_{\ell,(M-m_s)}(\theta_p)\mathcal{Y}_{\ell',(M-m_s)}(\theta_p)\langle\ell(M-m_s)Sm_s|JM\ell S\rangle\langle JM\ell' S|\ell'(M-m_s)Sm_s\rangle$$
$$\times\,|\langle Sm_s|(m_s-1/2)\,1/2\rangle|^2|\langle\mathcal{T}t_z|(t_z-1/2)\,1/2\rangle|^2. \tag{33}$$

Second-order anomalous derivative term. The numerator and denominator of the ADT contribution in Eq. (12) can be evaluated separately. From Eq. (5) it follows immediately that

$$\frac{\partial^2\Omega_0(\mu_0,T)}{\partial\mu_0^2} = -\frac{2M}{\pi^2}\int_0^\infty dp\, n_p, \tag{34}$$

and from Eq. (25) one gets

$$\frac{\Omega_{1,\mathrm{NN}}(\mu_0,T)}{\partial\mu_0} = \frac{2}{\pi^3}\int_0^\infty dp\, p^2\int_0^\infty dK\, K^2\frac{\partial\mathcal{F}(p,K)}{\partial\mu_0}\sum_{J,\ell,S}(2J+1)(2\mathcal{T}+1)\langle p|\tilde{V}_{\mathrm{NN}}^{J,\ell,\ell,S,\mathcal{T}}|p\rangle. \tag{35}$$

Here, the μ_0 derivative of $\mathcal{F}(p,K)$ is given by

$$\frac{\partial\mathcal{F}(p,K)}{\partial\mu_0} = \frac{\beta}{x}\left(2\frac{\ln(1+e^{\eta+2x})-\ln(e^{2x}+e^{\eta})}{(e^{\eta}-e^{-\eta})^2}+\frac{e^{\eta}(1-e^{4x})}{(e^{2\eta}-1)(e^{\eta}+e^{2x})(1+e^{\eta+2x})}\right), \tag{36}$$

where x and η are the same as in Eq. (26).

The numerical evaluation of the partial-wave representations of the second-order contributions at finite T was tested with model interactions of the one-boson exchange type [11]. With such a simple form of the interactions a semianalytical treatment at second order is possible.

E. Temperature- and density-dependent NN interaction

Up to now only the NN potential was considered in the second-order contributions. With three-nucleon forces included, the expressions for the second-order normal and anomalous contributions become somewhat involved. In zero-temperature many-body calculations it is common practice to approximate three-nucleon interactions at higher orders in perturbation theory by using a density-dependent effective two-nucleon (DDNN) potential [8,9,25,26]. This potential is constructed from the genuine three-body force by integrating out one nucleon line by summing over occupied states in the Fermi sea. For details regarding the construction we refer to Ref. [26]. Generalizing to finite temperatures, the following replacements have to be made in Eqs. (11), (12), and (17)–(26), of Sec. III A in Ref. [26]:

$$\frac{k_f^3}{3}\to\int_0^\infty dk\,k^2\left[1+\exp\frac{k^2/2M-\mu_0}{T}\right]^{-1} = -\sqrt{\frac{\pi}{2}}(MT)^{3/2}\mathrm{Li}_{3/2}(-e^{\mu_0/T}) = \frac{\pi^2}{2}\rho(\mu_0,T). \tag{37}$$

The integrals over one-pion propagator become

$$\Gamma_0(p) = \frac{1}{2p}\int_0^\infty dk\,k\left[1+\exp\frac{k^2/2M-\mu_0}{T}\right]^{-1}\ln\frac{m_\pi^2+(p+k)^2}{m_\pi^2+(p-k)^2}, \tag{38}$$

$$\Gamma_1(p) = \frac{1}{4p^3}\int_0^\infty dk\,k\left\{4pk-\left(m_\pi^2+p^2+k^2\right)\ln\frac{m_\pi^2+(p+k)^2}{m_\pi^2+(p-k)^2}\right\}\left[1+\exp\frac{k^2/2M-\mu_0}{T}\right]^{-1}, \tag{39}$$

$$\Gamma_2(p) = \frac{1}{16p^3}\int_0^\infty dk\,k\left\{4pk\left(m_\pi^2+p^2+k^2\right)-\left[m_\pi^2+(p+k)^2\right]\left[m_\pi^2+(p-k)^2\right]\right.$$
$$\left.\times\,\ln\frac{m_\pi^2+(p+k)^2}{m_\pi^2+(p-k)^2}\right\}\left[1+\exp\frac{k^2/2M-\mu_0}{T}\right]^{-1}, \tag{40}$$

$$\Gamma_3(p) = \frac{1}{16p^5}\int_0^\infty dk\,k\left\{-12pk\left(m_\pi^2+p^2+k^2\right)+\left[3\left(m_\pi^2+p^2+k^2\right)^2-4p^2k^2\right]\ln\frac{m_\pi^2+(p+k)^2}{m_\pi^2+(p-k)^2}\right\}\left[1+\exp\frac{k^2/2M-\mu_0}{T}\right]^{-1}, \tag{41}$$

while the integrals over the product of two different pion propagators are now given by

$$G_{0,*,**}(p,q) = \frac{2}{q}\int_0^\infty dk\,\frac{\{k,k^3,k^5\}}{\sqrt{A(p)+q^2k^2}}\left[1+\exp\frac{k^2/2M-\mu_0}{T}\right]^{-1}\ln\frac{qk+\sqrt{A(p)+q^2k^2}}{\sqrt{A(p)}}, \tag{42}$$

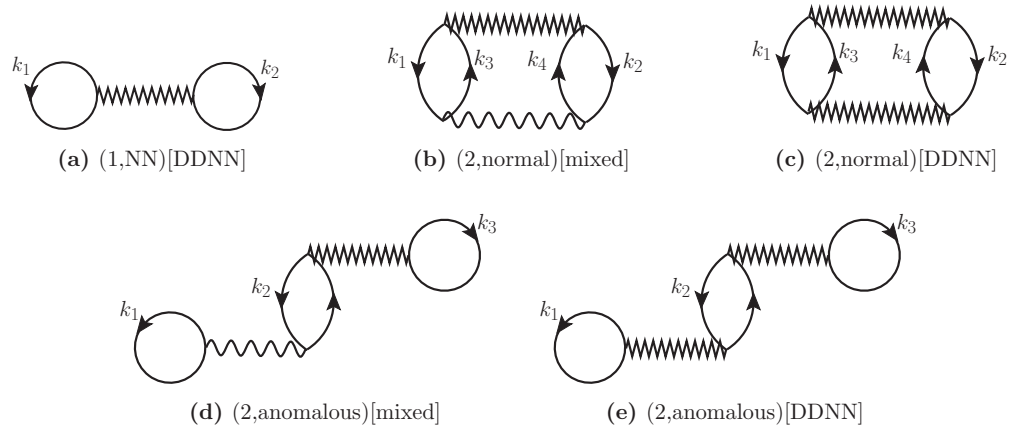

(a) (1,NN)[DDNN] (b) (2,normal)[mixed] (c) (2,normal)[DDNN]

(d) (2,anomalous)[mixed] (e) (2,anomalous)[DDNN]

FIG. 3. Antisymmetrized Goldstone diagrams representing the (a) first-order, (b) and (c) second-order normal, and (d) and (e) second-order anomalous contributions associated with the DDNN potential (represented by zigzag lines). The NN potential is symbolized by wavy lines. Diagram (a) carries an additional symmetry factor of 1/3, diagram (d) one of 1/2, and diagram (e) one of 1/4.

with $A(p) = [m_\pi^2 + (p+k)^2][m_\pi^2 + (p-k)^2]$. Note that Eqs. (19)–(22) in Ref. [26] which were set up to obtain the functions $G_{1,2,3}(p,q)$ remain valid.

In this approximation three-nucleon forces are included at second order by substituting for $\tilde{V}_{\rm NN}$ in Eqs. (28), (31), (32), and (35) the quantity $\tilde{V}_{\rm DDNN}(\rho,T)$ (the antisymmetrized temperature-dependent DDNN potential). When used in combination with $V_{\text{low-}k}(\Lambda)$ (i.e., in the VLK potential sets) the DDNN potential is constructed using the same sharp relative-momentum cutoff Λ, whereas when it is combined with the regularized chiral N3LO potentials (i.e., in the n3lo sets) the smooth regulator given in Eq. (1) is used. The diagrammatic representations of the additional second-order normal and anomalous contributions arising from $\tilde{V}_{\rm DDNN}(\rho,T)$ are depicted in Fig. 3.

To test the quality of the DDNN approximation we compare in Figs. 4(a) and 4(b) the results for the first-order three-body contribution calculated with genuine 3N forces with the results obtained using $\tilde{V}_{\rm DDNN}(\rho,T)$ in the first-order NN contribution, Eq. (27). The quantity shown is the free energy per nucleon $\bar{F}(\rho,T) = \rho^{-1}F(\rho,T)$ as a function of density for temperatures $T = 0,25$ MeV. The insets magnify the behavior in the low- and the high-density region, respectively. Incidentally one sees that the Nijmegen LECs used in the interaction sets involving $V_{\text{low-}k}$ potentials [Fig. 4(a)] lead to considerably larger 3N contributions at first order in MBPT. For sharp regulators the T dependence of the first-order DDNN contributions is similar to the results obtained with genuine 3N forces. For the relatively soft $n = 2$ regulator this is not the case in the high-density region, as can be seen in Fig. 4(b) where the results for n3lo500 are shown. Nevertheless, the deviations are in all cases small enough to justify using $\tilde{V}_{\rm DDNN}(\rho,T)$ instead of the genuine three-body potential at second order.

Figures 5(a)–5(d) show the results for the different second-order normal contribution arising from $\tilde{V}_{\rm NN}$ and $\tilde{V}_{\rm DDNN}(\rho,T)$. Here, $\bar{F}_{2,\rm normal}$[NN] denotes the contribution where both interactions are $\tilde{V}_{\rm NN}$, $\bar{F}_{2,\rm normal}$[mixed] is the case where one interaction is given by $\tilde{V}_{\rm NN}$ and the other one by $\tilde{V}_{\rm DDNN}(\rho,T)$, and $\bar{F}_{2,\rm normal}$[DDNN] denotes the case where both interactions are $\tilde{V}_{\rm DDNN}(\rho,T)$. Furthermore, we define $\bar{F}_{2,\rm normal}[\text{total}] = \bar{F}_{2,\rm normal}[\text{NN}] + \bar{F}_{2,\rm normal}[\text{mixed}] + \bar{F}_{2,\rm normal}[\text{DDNN}]$.

One sees that the size of the two-body contribution $\bar{F}_{2,\rm normal}$[NN] increases with the resolution scale. Among the different NN potentials, n3lo500 gives rise to the largest second-order normal contribution. For n3lo450 and VLK23 (not shown) as well as for n3lo414 and VLK21 the results for $\bar{F}_{2,\rm normal}$[NN] are almost the same and feature nonmonotonic behavior as the density and temperature increase. In contrast, similar to the first-order 3N contributions, the pure DDNN contributions $\bar{F}_{2,\rm normal}$[DDNN] exhibit a continuous increase in magnitude with density as well as with temperature. The size of the $\bar{F}_{2,\rm normal}$[DDNN] contribution is noticeably larger for VLK21 (and for VLK23). The size of the sum of the total additional DDNN contributions, $\bar{F}_{2,\rm normal}$[mixed] + $\bar{F}_{2,\rm normal}$[DDNN], is then also the largest in that case. In the other cases $\bar{F}_{2,\rm normal}$[DDNN] is of comparable size. In the case of n3lo500 it is additionally suppressed by the mixed contribution $\bar{F}_{2,\rm normal}$[mixed], leading to an overall relatively small modification of the second-order normal contribution when three-body forces are included. The different sizes of the additional DDNN contributions at second order for different potentials underlie most of the discussion in Sec. IV A.

F. Results for anomalous contributions

With $\tilde{V}_{\rm DDNN}(\rho,T)$ included there are three different second-order anomalous contributions. The one where both interactions are $\tilde{V}_{\rm NN}$ is denoted by $\bar{F}_{2,\rm anomalous}$[NN], the one with two $\tilde{V}_{\rm DDNN}(\rho,T)$-type interactions is denoted by $\bar{F}_{2,\rm anomalous}$ [DDNN], and the case where one interaction is given by $\tilde{V}_{\rm NN}$ and the other one by $\tilde{V}_{\rm DDNN}(\rho,T)$ is denoted by $\bar{F}_{2,\rm anomalous}$[mixed]. As can be seen in Fig. 6, the size of these contributions is relatively large; in fact, in the high-density domain these are, together with the respective anomalous derivative terms, the largest contributions in the Kohn-Luttinger-Ward formula, Eq. (12). However, the total anomalous contributions, i.e., $\bar{F}_{\rm totanom}[\cdots] = \bar{F}_{2,\rm anomalous}[\cdots] + \bar{F}_{\rm ADT}[\cdots]$, are relatively small in size and (as expected) decrease with temperature.

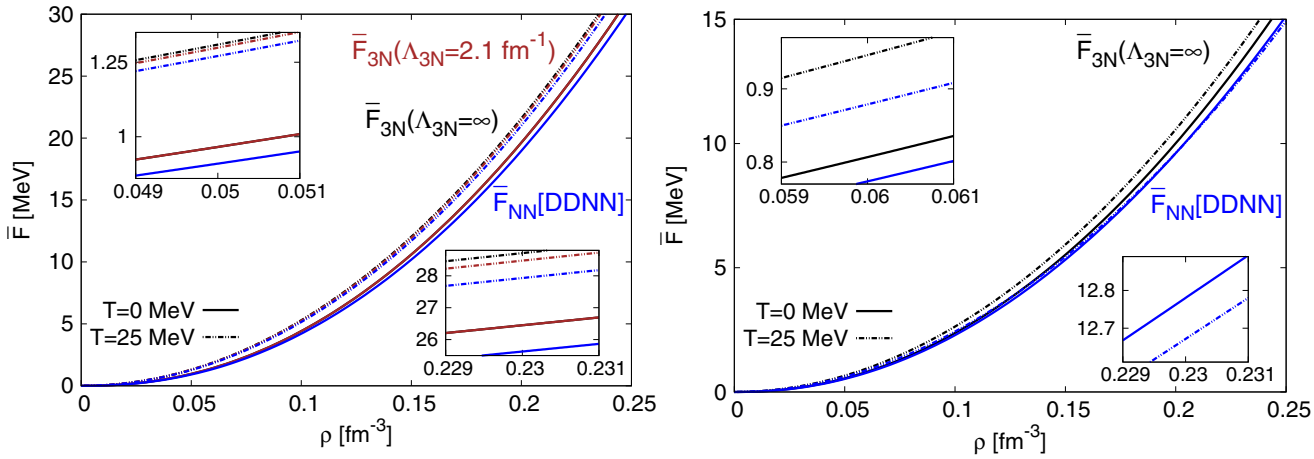

(a) VLK21 (b) n3lo500

FIG. 4. (Color online) First-order three-body contribution to the free energy per nucleon calculated with genuine 3N forces, $\bar{F}_{3N}$, and with the temperature- and density-dependent effective nucleon-nucleon (DDNN) potential, $\bar{F}_{NN}$[DDNN]. In Fig. 4(a) we show also the results when a Jacobi momentum regulator with $\Lambda_{3N} = 2.1$ fm^{-1} is used for the genuine 3N contribution.[3] At zero temperature the results for $\bar{F}_{3N}(\Lambda_{3N} = \infty)$ and $\bar{F}_{3N}(\Lambda_{3N} = 2.1\,\text{fm}^{-1})$ overlap.

G. Self-energy contributions to the single-nucleon energies

The single-nucleon energies ε_k appear explicitly in the second-order normal contributions, Eq. (15). The exact propagator $G(k,\omega)$ is defined by the self-consistent Dyson equation, which can be resummed as a geometric series:

$$G(k,\omega) = G_0(k,\omega) + G_0(k,\omega)\,\Sigma(k,\omega)\,G(k,\omega) = \left[\omega - \frac{k^2}{2M} - \Sigma(k,\omega)\right]^{-1}. \quad (43)$$

Using the temperature-dependent DDNN potential approximation for three-body forces, the first-order contribution to the proper self-energy (expanded in partial waves) reads

$$\Sigma_1(k;\mu_0,T) = \frac{1}{4\pi}\int_0^\infty dq\, q^2\, n_q \int_{-1}^{1} d\cos\theta_q \sum_{J,\ell,S}(2J+1)(2\mathcal{T}+1) \times \left\langle \frac{|\vec{k}-\vec{q}|}{2}\right| \tilde{V}_{\rm NN}^{J,\ell,\ell,S,\mathcal{T}} + \frac{1}{2}\tilde{V}_{\rm DDNN}^{J,\ell,\ell,S,\mathcal{T}} \left|\frac{|\vec{k}-\vec{q}|}{2}\right\rangle, \quad (44)$$

where θ_p is the angle between $\vec{q}$ and $\vec{k}$. The DDNN interaction carries an additional symmetry factor of $1/2$. Nucleon self-energies can be easily included using the effective-mass approximation:

$$\varepsilon(k;\rho,T) = \frac{k^2}{2M} + \Sigma(k;\rho,T) \simeq \frac{k^2}{2M^*(\rho,T)} + U_0(\rho,T), \quad (45)$$

where $M^*(\rho,T)$ is called the (density- and temperature-dependent) effective mass. The momentum independent parts $U_0(\rho,T)$ of the single-nucleon energies cancel in Eq. (15), and therefore it suffices to multiply the partial-wave expanded expressions in Eqs. (28) and (31) with a factor $M^*(\rho,T)/M$ to incorporate self-energy effects. We show the size of this effective-mass factor for different temperatures and interactions in Fig. 7. One sees that $M^*(\rho,T)/M$ decreases with density and increases with temperature and that $M^*/M \leqslant 1$. Hence, including the effective-mass factors leads to a reduction of the different second-order normal contributions. When represented as a function of the one-body chemical potential μ_0 the $M^*(\mu_0,T)/M$ curves all cross at approximately the same point for each set of two- and three-body potentials, which is not directly apparent from Eqs. (44) and (45). Higher-order contributions to the nucleon single-particle energies at or near zero temperature have been calculated from chiral nuclear interactions in Refs. [8,14,46,47]. Extending these calculations to the temperature region $T \leqslant 25$ MeV considered in this work will be the subject of future research.

IV. RESULTS

In this section we examine the results for the thermodynamic equation of state of isospin-symmetric nuclear matter, calculated using all of the different contributions presented in the previous section. The convergence behavior of the many-body perturbation series and the model dependence of the different contributions is investigated, and we then examine the (physical) equations of state resulting from the n3lo500, n3lo450, and n3lo414 potential sets.

A. Convergence of the perturbation series

In Fig. 8 we examine the convergence behavior of the zero- and finite-temperature perturbation series for the different potential sets listed in Table I. Figures 8(a) and 8(b) show

[3]To be precise, the regulator used to calculate the brown curves is given by $f(a,b) = \exp[-(a^2 + \frac{3}{4}b^2)^2/\Lambda_{3N}^4]$, where $a = \frac{1}{2}|k_1 - k_2|$ and $b = \frac{2}{3}|k_3 - \frac{1}{2}(k_1 + k_2)|$. As this regulator is more restrictive than the usual one where a and b are given by absolute values of (proper) Jacobi momenta, i.e., $a = |\vec{P}|$ and $b = |\vec{Q}|$, the effects of the latter are even smaller.

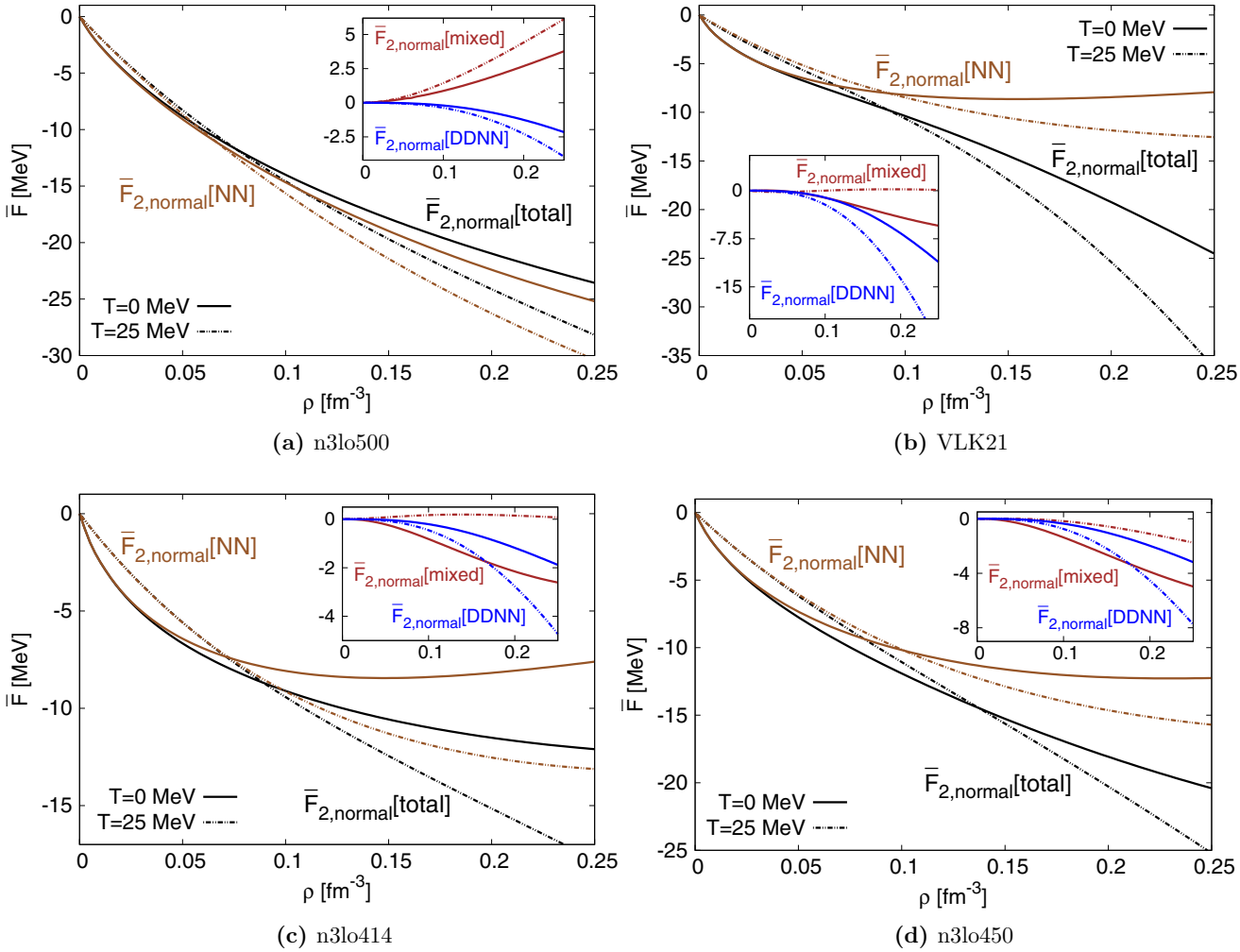

(a) n3lo500 (b) VLK21

(c) n3lo414 (d) n3lo450

FIG. 5. (Color online) Second-order normal contributions from different potential sets. The insets show the contributions which arise from the temperature- and density-dependent NN interactions.

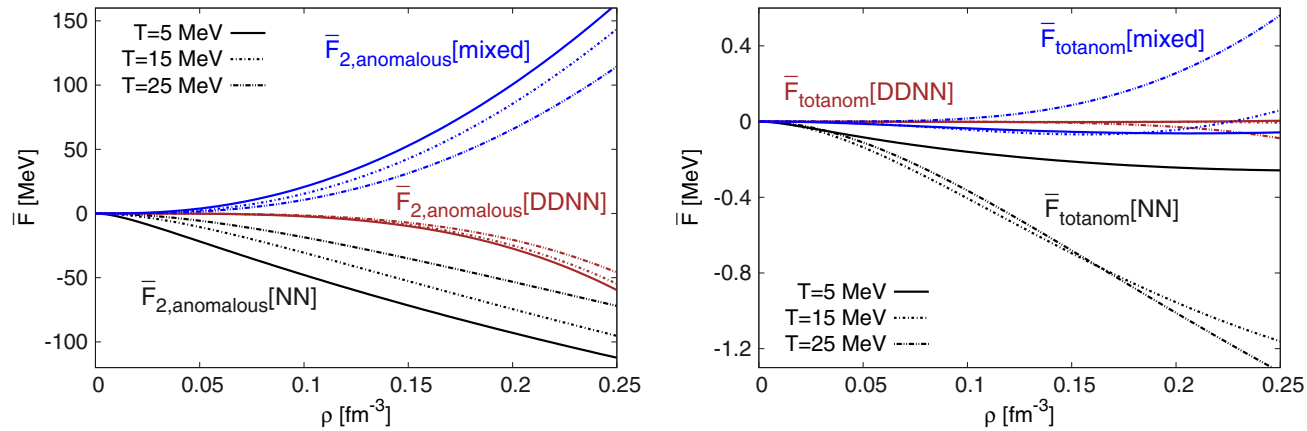

FIG. 6. (Color online) Second-order anomalous contributions arising from $\tilde{V}_{\rm NN}$ and $\tilde{V}_{\rm DDNN}(\rho,T)$, and the corresponding contributions when the respective anomalous derivative terms are added, calculated using n3lo450.

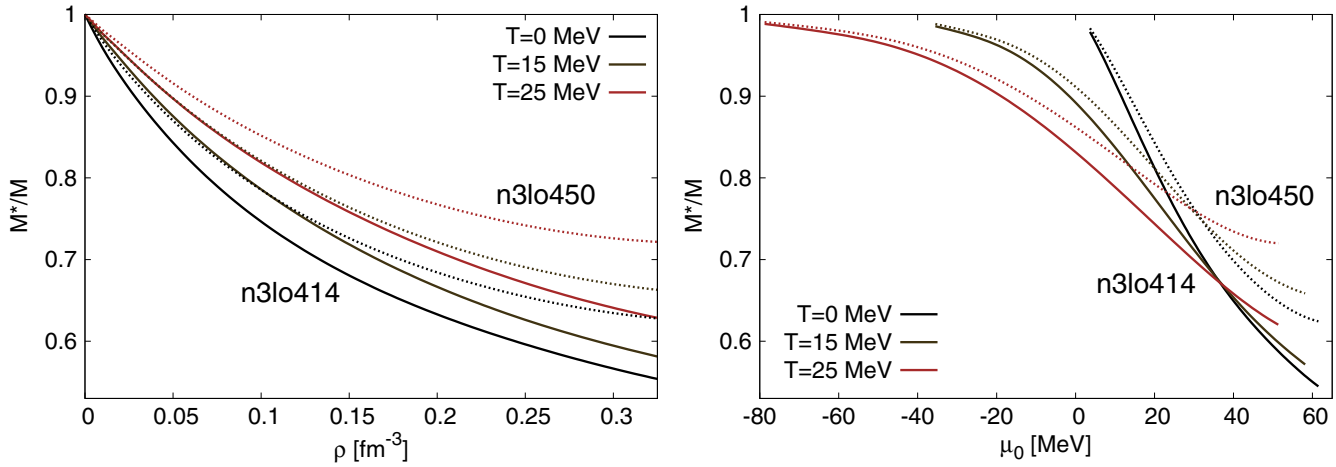

FIG. 7. (Color online) Effective-mass ratio M^*/M from n3lo414 (solid lines) and n3lo450 (dashed lines) as a function of the nucleon density ρ and the one-body chemical potential μ_0, respectively, for different temperatures.

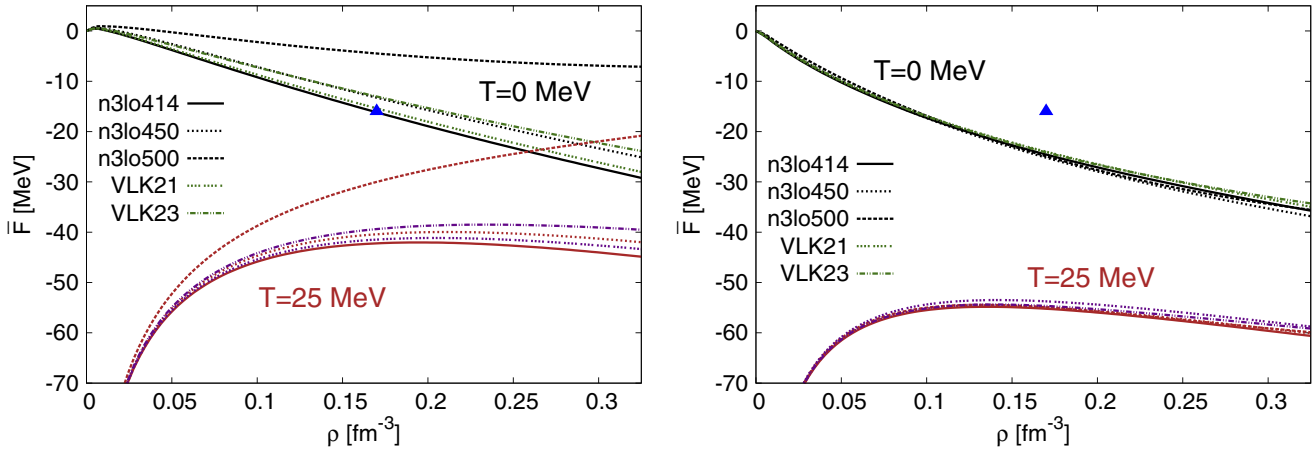

(a) NN first order, no 3N

(b) NN second order, no 3N

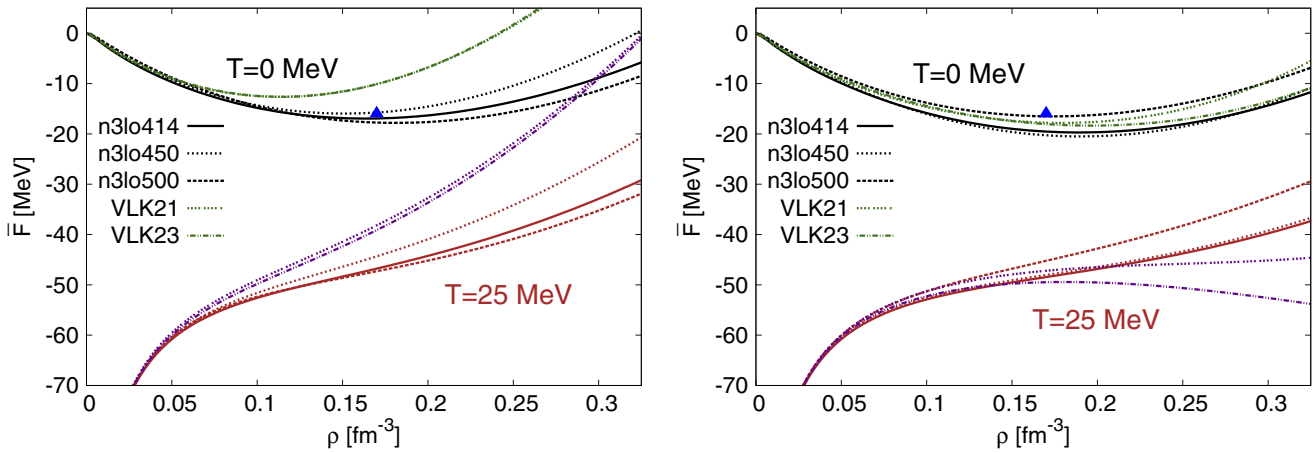

(c) NN second order, 3N first order

(d) NN second order, 3N second order

FIG. 8. (Color online) Free energy per nucleon $\bar{F}(\rho,T)$ at different stages in MBPT, calculated using different low-momentum interactions. The blue triangle marks the empirical saturation point $\bar{E}_0 \simeq -16\,\mathrm{MeV}$, $\rho_0 \simeq 0.17\,\mathrm{fm}^{-3}$.

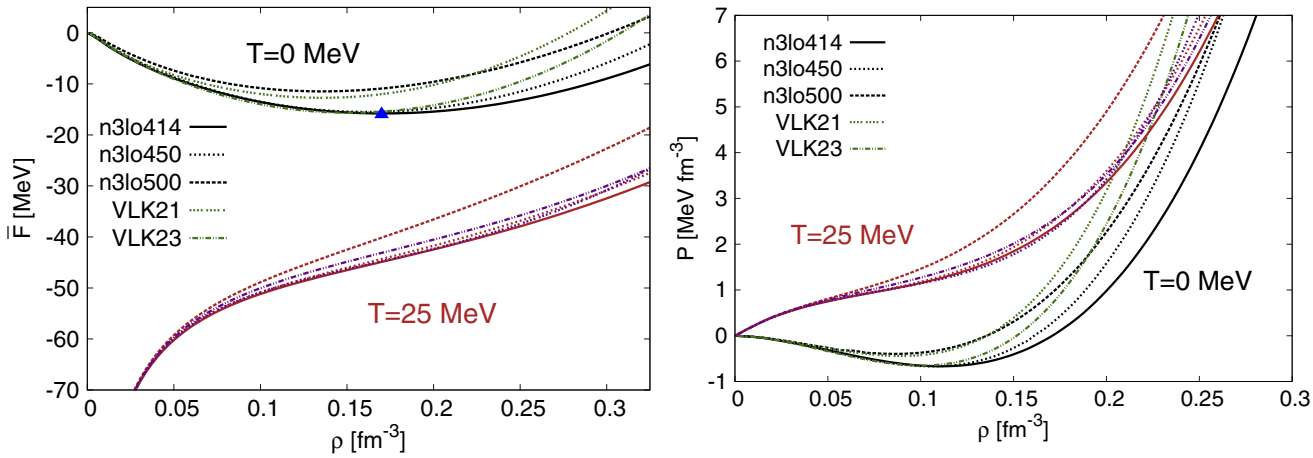

FIG. 9. (Color online) Free energy per nucleon $\bar{F}(\rho,T)$ and pressure isotherms $P(\rho,T)$ for isospin-symmetric nuclear matter at second order in MBPT, with the effective-mass factors M^*/M included. Only the pressure isotherms from VLK21 and the ones from VLK23 (green and purple curves) cross each other.

the results for the free energy per nucleon $\bar{F}(\rho,T)$ for the case when only two-body forces are considered. While the first-order results from n3lo450 and VLK23 as well as the ones from n3lo414 and VLK21 are of similar size, the free energy per nucleon calculated from n3lo500 is significantly smaller in magnitude. In fact, for n3lo500 the first- and the second-order NN contributions are of comparable size, which points to the decreased perturbative quality of this two-body potential [19]. Even so, at second order (with NN forces only) the scale dependence is significantly reduced, and similar results are obtained with all five interactions sets.

The results deviate again when three-nucleon forces are included at first order, as can be seen in Fig. 8(c), which is entirely from the deviating values of the five low-energy constants that parametrize the 3N potential. The deviations among the n3lo results (and similarly among the VLK results) are visible, but significantly smaller than the difference between VLK and n3lo results (particularly the VLK results at zero temperature are almost identical at this order). Finally, in Fig. 8(d) the second-order DDNN contributions are included. Here the results become again more model independent, but only in the case of zero temperature. At finite T the curves for $\bar{F}(\rho,T)$ are now considerably flatter in the case of VLK21 and especially VLK23 as compared to the n3lo results. The reason for this behavior is the different size of the total second-order normal three-body contribution $\bar{F}_{2,\mathrm{normal}}[\mathrm{mixed}] + \bar{F}_{2,\mathrm{normal}}[\mathrm{DDNN}]$ in each case, cf. Figs. 5(a)–5(d). This contribution is much larger for the VLK potential sets. At zero temperature it balances the large first-order 3N contribution caused by the Nijmegen LECs, leading to results similar to those of the n3lo LECs. Because of the much more pronounced temperature dependence of the second-order DDNN contributions (as compared to the first-order three-body contribution) there is overcompensation at finite T, leading to the observed flattening of the $\bar{F}(\rho,T)$ curves with increasing temperature. A similar (but more moderate) flattening occurs also in the high-density domain of the results obtained from n3lo450 and n3lo414. It is entirely absent in the case of n3lo500, where the respective contribution is small (and has opposite sign). Because the pressure is defined as $P(\rho,T) = \rho^2 \partial \bar{F}(\rho,T)/\partial\rho$, the flattening present in the VLK results leads to crossing pressure isotherms. Ultimately, the origin of this behavior lies in the large values of the Nijmegen LECs.

In Fig. 9 we show the second-order results with the effective-mass factors M^*/M included. The flatness problem of the finite temperature VLK curves is no longer present, and at $T = 25$ MeV the VLK results and the ones obtained from n3lo450 and n3lo414 are in close agreement. At zero temperature nuclear matter is under-bound with the VLK21 potential ($\bar{E}_0 = -12.73$ MeV), the saturation density is somewhat small ($\rho_0 = 0.136\,\mathrm{fm}^{-3}$), and the compressibility is $K = 200$ MeV. For VLK23 the saturation point is close to the empirical value, i.e., $\bar{E}_0 = -15.66$ MeV and $\rho_0 = 0.152\,\mathrm{fm}^{-3}$, and the compressibility $K = 260$ MeV is in agreement with empirical constraints (see Sec. IV B). However, for both VLK21 and VLK23 the zero-temperature curves are now somewhat steep for densities just above saturation density, and the crossing of the pressure isotherms is therefore still present as can be seen in the second plot in Fig. 9.[4] From $\partial P/\partial T = \alpha/\kappa_T$ (where $\kappa_T \geqslant 0$ is the isothermal compressibility) it follows that this crossing implies a large negative coefficient of thermal expansion α, i.e., there would be a large decrease in pressure when the temperature is increased at fixed density. In the case of n3lo450 and n3lo414 the pure second-order calculation resulted in nuclear matter that was over-bound at low temperatures. The first-order corrections to the single-particle energies reduces the strong attraction in the second-order normal diagram and improves the description of nuclear matter at zero temperature for the n3lo414 and n3lo450 potentials. By contrast, with n3lo500 the saturation point is only reproduced in the pure second-order calculation (without the effective-mass corrections). The agreement is likely coincidental, and higher-order perturbative contributions should be included [19].

[4] A fully consistent RG treatment including induced many-nucleon forces may help cure this feature. See Refs. [39,48,49] for additional details.

B. Equation of state of isospin-symmetric nuclear matter

In the following we examine the properties of the nuclear matter equations of state that result from the chiral nuclear interactions n3lo414, n3lo450, and n3lo500. Both the n3lo414 and n3lo450 potentials are well converged at second order in perturbation theory with self-consistent single-particle energies [19], while higher-order contributions to the free energy per particle are required to achieve convergence with the n3lo500 two-body potential. For comparison, we compute the thermodynamics of nuclear matter from n3lo500 *without effective-mass contributions* only to study whether universal features at finite temperature can arise starting from realistic zero-temperature equations of state.

From the free energy per nucleon $\bar{F}(\rho,T)$ all other thermodynamic quantities follow by standard thermodynamic relations. The pressure $P(\rho,T)$ and the (nonrelativistic) chemical potential $\mu(\rho,T)$, for instance, are given by

$$P(\rho,T) = \rho^2 \frac{\partial \bar{F}(\rho,T)}{\partial \rho}, \tag{46}$$

$$\mu(\rho,T) = \bar{F}(\rho,T) + \rho \frac{\partial \bar{F}(\rho,T)}{\partial \rho}. \tag{47}$$

The numerical results for $\bar{F}(\rho,T)$ and $P(\rho,T)$ are shown in Fig. 10 for densities $\rho < 0.35\,\mathrm{fm}^{-3}$ and temperatures in the region $T = 0{-}25$ MeV for all three n3lo potential sets. Additional derived thermodynamic quantities are shown for n3lo414 in Fig. 11, i.e., free energy density $F(\rho,T)$, chemical potential $\mu(\rho,T)$, and pressure $P(\mu,T)$.

Liquid-gas phase transition. For temperatures below a critical value T_c the analytical free energy density at fixed temperature $F(\rho,T) = \rho\bar{F}(\rho,T)$ exhibits a mechanically unstable region of negative curvature,[5] which signifies the presence of a first-order phase transition. The physical equation of state inside the transition region is obtained by performing the Maxwell construction. In the following we briefly recall the properties of the equation of state associated with this method.

From the nonconvexity of the free energy density $F(\rho,T)$ it follows that the chemical potential and pressure isotherms are nonmonotonic (as functions of ρ). This implies that for temperatures $T < T_c$ there exist points $(\rho_a(T), F_a(T))$ and $(\rho_b(T), F_b(T))$ which have matching values of these quantities [denoted by $\mu_m(T)$ and $P_m(T)$] and therefore represent systems that can coexist in mutual thermodynamic equilibrium. These points delineate the region in which the low density, the gaslike (in analogy to classical gases described by the van der Waals equation of state), and the high density, the liquidlike phase, mix.

In the regions adjacent to (ρ_a, F_a) and (ρ_b, F_b) where the free energy density is still convex the system is mechanically metastable, i.e., a finite disturbance is needed to induce phase separation, whereas in the inner region of thermodynamic instability the system separates spontaneously.

[5]Nonconvexity of $F(\rho,T)$ with respect to ρ implies a negative isothermal compressibility κ_T which violates the stability relation $\kappa_T \geqslant 0$.

The values of $\mu_m(T)$ and $P_m(T)$ are obtained by constructing double tangents in the $\bar{F}(v,T)$ plots (where $v = 1/\rho$ is the volume per nucleon), i.e., for fixed temperature $T < T_c$ one finds values v_a and v_b (where $v_a > v_b$) for which

$$\bar{F}(v_a,T) - \bar{F}(v_b,T) = -P_m(T)(v_a - v_b), \tag{48}$$

$$\left.\frac{\partial \bar{F}(v,T)}{\partial v}\right|_{v_a,v_b} = -P_m(T). \tag{49}$$

The points specified by these equations are identical to the ones with equal values of pressure and chemical potential. The free energy per nucleon of the liquid-gas mixture is then given by substituting the analytical results with the double tangents,[6] i.e., for $\rho \in [\rho_a(T), \rho_b(T)]$ and $T < T_c$ it is

$$\bar{F}(\rho,T) = \mu_m(T) - \frac{P_m(T)}{\rho}. \tag{50}$$

The physical equations of state resulting from this construction are given by the solid lines in Figs. 10 and 11. Because the Maxwell construction does not preserve the curvature of $\bar{F}(\rho,T)$ at the boundaries $\{\rho_a(T), \rho_b(T)\}$ of the transition regions, both $P(\rho,T)$ and $\mu(\rho,T)$ are not differentiable at these points. For $\rho \in [\rho_a(T), \rho_b(T)]$ the chemical potential and the pressure are constant and their values given by $\mu_m(T)$ and $P_m(T)$, respectively. Hence, in the physical $P(\mu,T)$ diagrams the regions of phase coexistence collapse to single points with coordinates $(P_m(T), \mu_m(T))$. The different parts of the region of thermodynamic instability are particularly exposed in the analytical $P(\mu,T)$ curves. Here, the transition from mechanical metastability to the unstable region with nonconvex free energy density is marked out by sharp bends and for $T < T_c$ the analytical $P(\mu,T)$ diagrams become triple valued (double valued at zero temperature). The regions of phase coexistence terminate at the critical point (P_c, ρ_c, T_c) where both derivatives of the pressure vanish (signifying a second-order transition point):

$$\left.\frac{\partial P(\rho,T)}{\partial \rho}\right|_{T=T_c,\,\rho=\rho_c} = \left.\frac{\partial^2 P(\rho,T)}{\partial \rho^2}\right|_{T=T_c,\,\rho=\rho_c} = 0. \tag{51}$$

For pressures above the critical value P_c there is no phase transition from a dense liquidlike to a low-density gaslike phase; nuclear matter instead behaves as a fluid whose properties vary continuously with temperature.

Zero-density limit. In the limit of vanishing density the interactions between nucleons vanish and $\bar{F}_0 = \mu_0 + \Omega_0/\rho$ gives the dominant contribution to the free energy per nucleon.

[6]The concentrations of the liquid and the gas part in the phase separated system are given by $c_{\mathrm{liquid}}(v) = \frac{v-v_b}{v_a-v_b}$ and $c_{\mathrm{gas}}(v) = \frac{v_a-v}{v_a-v_b}$, respectively, so the free energy per nucleon of the mixture coincides with the one given by the double tangents, $c_{\mathrm{liquid}}(v)\bar{F}(v_a,T) + c_{\mathrm{gas}}(v)\bar{F}(v_b,T) = \bar{F}(v_b,T) - P_m(T)(v - v_b)$. Note that negative curvature of $F(\rho,T)$ corresponds to concavity of $\bar{F}(v,T)$ (at fixed T), so the double tangents lie underneath the analytical results and the free energy density of the mixture is smaller than that of the unseparated system.

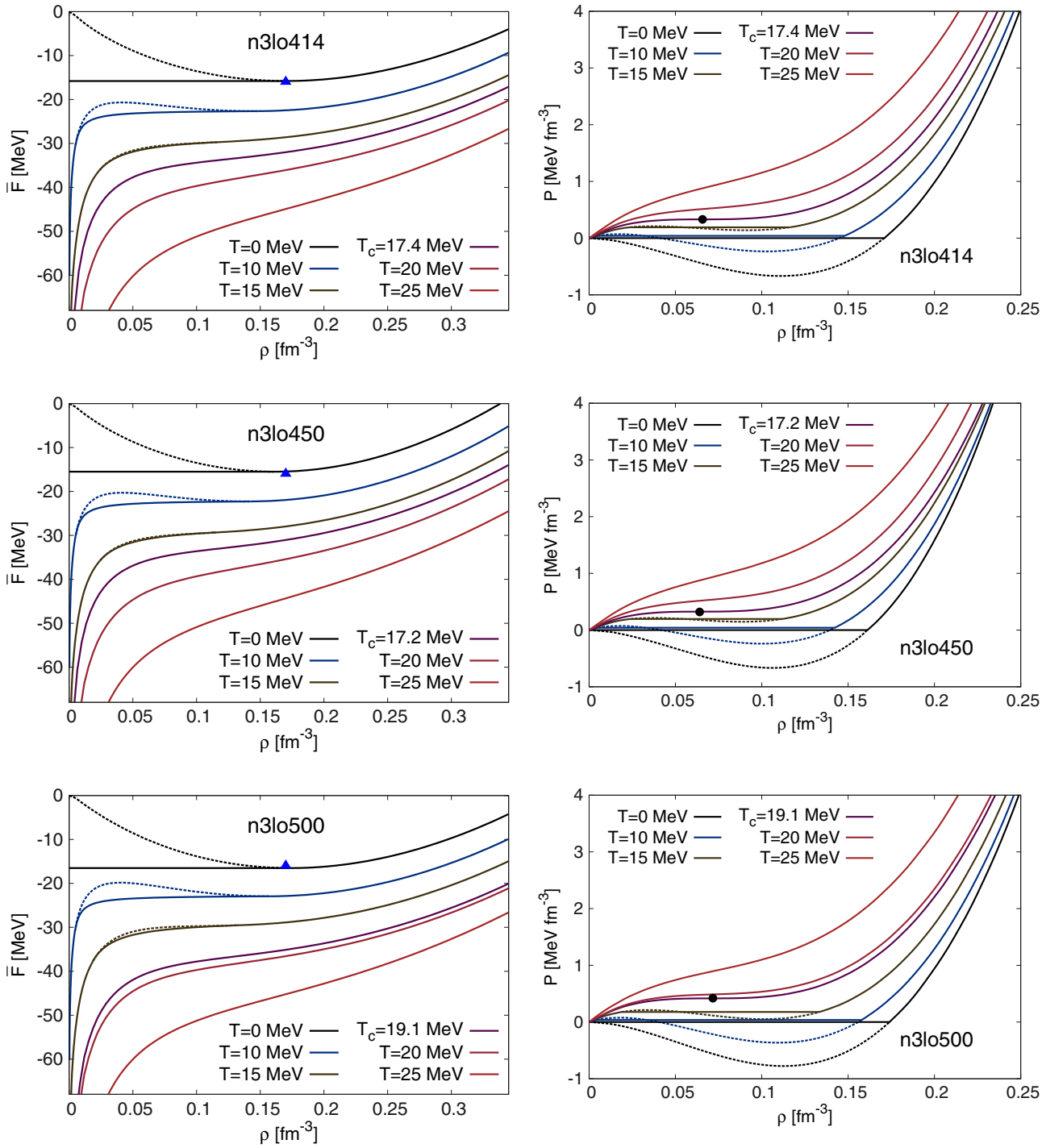

FIG. 10. (Color online) Free energy per nucleon $\bar{F}(\rho,T)$ and pressure $P(\rho,T)$ for isospin-symmetric nuclear matter, calculated with the n3lo potential sets. The dashed lines show the analytical results, the solid lines the physical equations of state (obtained with the Maxwell construction). The blue triangle marks the empirical saturation point, and the black dot the critical point resulting from the respective potential sets.

The singular behavior of the $\bar{F}(\rho,T)$ curves for $\rho \to 0$ at nonzero temperature is therefore entirely caused by the noninteracting contribution $\bar{F}_0$. The leading term in Eq. (4) can be written as

$$\Omega_0(\mu_0,T) = \sqrt{2}\,T \left(\frac{M}{\beta\pi}\right)^{\frac{3}{2}} \mathrm{Li}_{5/2}(-\exp(\beta\mu_0)). \tag{52}$$

With the corresponding expression for $\rho(\mu_0,T)$ in Eq. (5) and $\mu_0 \xrightarrow{\rho\to 0} -\infty$ it follows that

$$\bar{F}_0(\mu_0,T) = \mu_0 - T\frac{\mathrm{Li}_{5/2}(-\exp(\beta\mu_0))}{\mathrm{Li}_{3/2}(-\exp(\beta\mu_0))} \xrightarrow{\mu_0\to-\infty} \mu_0 - T. \tag{53}$$

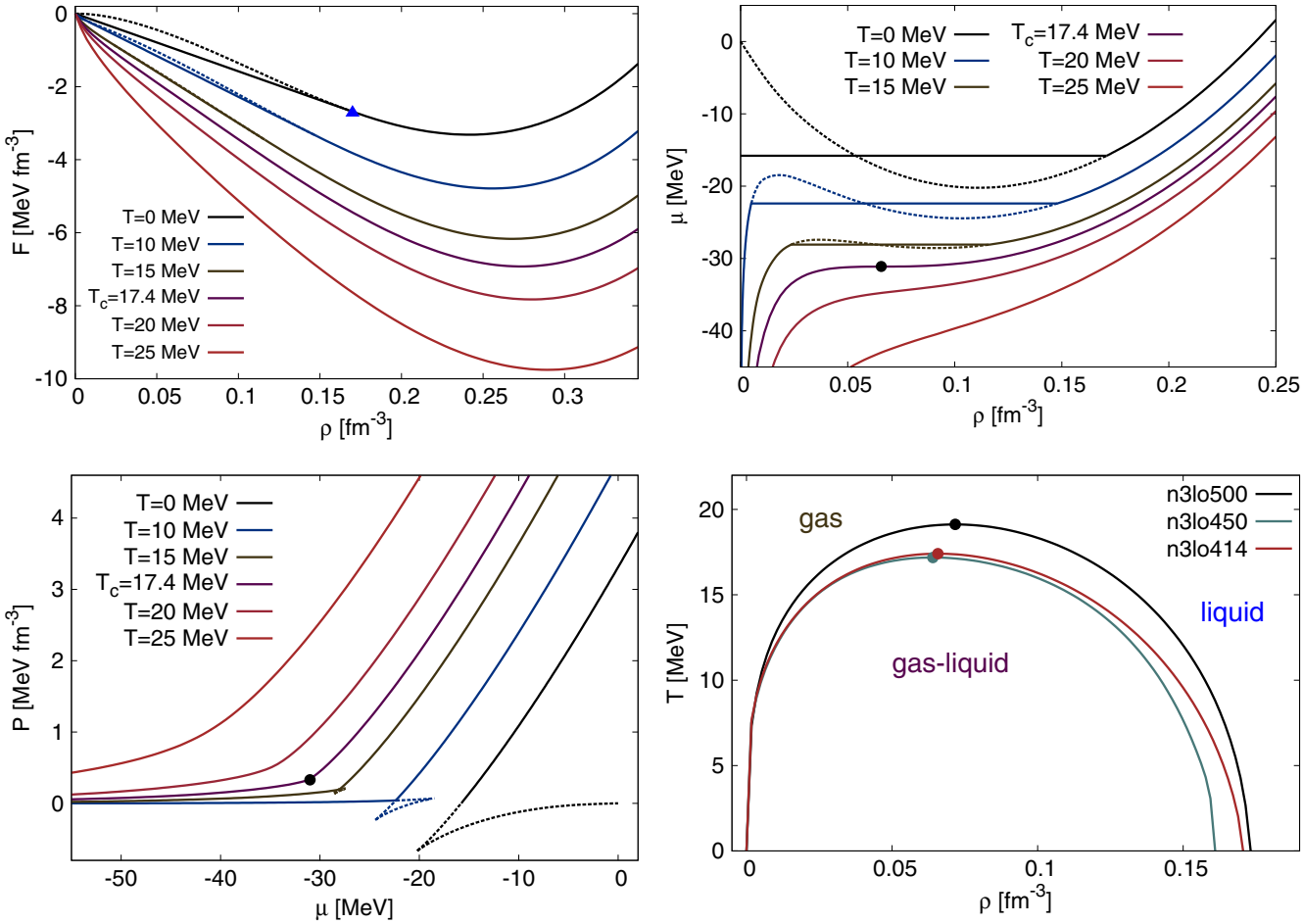

FIG. 11. (Color online) Free energy density $F(\rho,T)$, chemical potential $\mu(\rho,T)$, and pressure as a function of chemical potential $P(\mu,T)$ from n3lo414, as well as the $T-\rho$ phase diagram from n3lo500, n3lo450, and n3lo414. In the first three plots the dashed lines show the analytical results and the solid lines the physical equation of state. The blue triangle and the (black) dot(s) mark the empirical saturation point and the determined critical point(s), respectively.

Returning to Eq. (6) this shows that the singularity of the free energy per nucleon is logarithmic, $\sim \ln\rho$. Hence, despite the divergent behavior of $\bar{F}(\rho,T)$, the free energy density $F(\rho,T)=\rho\bar{F}(\rho,T)$ vanishes in the $\rho\to 0$ limit (cf. Fig. 11). Furthermore, the limiting behavior of the entropy per nucleon is given by

$$\bar{S}(\rho,T) = -\frac{\partial\bar{F}(\rho,T)}{\partial T} \xrightarrow{\rho\to 0} \frac{5}{2} - \frac{\mu_0(\rho,T)}{T}. \qquad (54)$$

This shows that the total internal energy per nucleon $\bar{E}=\bar{F}+T\bar{S}$ approaches the value $3T/2$ for $\rho\to 0$, which corresponds to the equation of state of a classical ideal gas.

It should be noted here that in the low-density region the picture of nuclear matter as a homogeneous system is incomplete. This follows from the fact that at densities well below saturation density few-body correlations as well as Coulomb repulsion of protons are important. Light clusters such as deuterons, tritons, and α particles are formed. Because of the Pauli principle these clusters dissolve at higher densities, yet they can still be expected to play a role when it comes to the liquid-gas phase transition. A detailed study of cluster formation and its effects on the nuclear EoS was provided by Typel *et al.* [50]. Their results suggest only modest changes regarding the position of the critical point, such as a shift of T_c by less then 10% from nucleonic clustering.

Nuclear bulk properties and thermodynamic observables. In Table II we give the values of several key quantities that characterize the obtained equations of state. The empirical saturation point $(\bar{E}_0,\rho_0)\simeq(-16\,\text{MeV},0.17\,\text{fm}^{-3})$ is best reproduced by n3lo414, but all potential sets lead to acceptable agreement. Also the empirical value of the compressibility [51–53],

$$K = 9\rho_0^2\left.\frac{\partial^2\bar{E}(\rho)}{\partial\rho^2}\right|_{\rho=\rho_0} = 250\pm 25\,\text{MeV}, \qquad (55)$$

comes out correctly for all sets of potentials. The critical point lies higher for n3lo500, and is very similar for the n3lo450 and n3lo414 results. The most recent empirical values for its coordinates have been obtained by the study of data from multifragmentation and compound nuclear decay experiments by Elliot *et al.* [5]; their values $T_c=17.9\pm 0.4\,\text{MeV}$, $\rho_c=0.06\pm 0.02\,\text{fm}^{-3}$, $P_c=0.31\pm 0.07\,\text{MeV fm}^{-3}$ are in

TABLE II. Saturation point $(\bar{E}_0, \rho_0)$, compressibility K, and critical values of temperature T_c, density ρ_c, and pressure P_c resulting from the equations of state obtained with the n3lo potentials.

	$\bar{E}_0$ (MeV)	ρ_0 (fm^{-3})	K (MeV)	T_c (MeV)	ρ_c (fm^{-3})	P_c (MeV fm^{-3})
n3lo500 (no M^*/M)	–16.51	0.174	250	19.1	0.072	0.42
n3lo450 (M^*/M)	–15.50	0.161	244	17.2	0.064	0.32
n3lo414 (M^*/M)	–15.79	0.171	223	17.4	0.066	0.33

agreement with previous studies by Karnaukhov *et al.* [6], and agree more closely with the n3lo450 and n3lo414 results.

Phase diagram. In Fig. 11 we show the $T-\rho$ phase diagrams resulting from n3lo500, n3lo450, and n3lo414. As a consequence of the third law of thermodynamics, the boundaries of the coexistence region $(\rho_a(T), \rho_b(T))$ must approach the ρ axis with infinite slope. At zero temperature there is no pure gas phase, and the boundary points are given by $(0, \rho_0)$. Above the critical temperature there is only the gaslike phase.

C. Discussion of results

We have seen that the differences in the results obtained from different potential sets are predominantly from the contributions associated with the three-body interactions, which depend sensitively on the choice of low-energy constants c_E, c_D, and $c_{1,3,4}$. The dominant three-body contributions are the ones which are proportional to c_3, and the crossing of pressure isotherm present in the VLK21 and VLK23 results can be linked mainly to the large value of this low-energy constant in the Nijmegen LECs.

It should be stressed that in our calculation we have used leading-order (with respect to the chiral expansion) three-body forces only. The subleading (N3LO) 3N forces and the leading 4N forces have so far been fully included only in neutron matter calculations [10,13] at zero temperature. In nuclear matter already the leading-order 3N force is more intricate; in addition to the vanishing of all contributions proportional to c_E, c_D, and c_4, in pure neutron matter the two-pion exchange kernels given in Eqs. (20) and (21) are decreased by factors $1/12$ and $1/6$, respectively.[7] Initial investigations have shown that chiral four-body forces can give contributions to the nuclear equation of state of considerable size, but substantial cancellations among the contributions from N3LO many-nucleon forces have been conjectured [54]. It remains a future task to fully include higher-order many-nucleon forces in nuclear matter calculations.

The potentials considered in the present work that best reproduce bulk properties of symmetric nuclear matter at zero temperature also give comparable results at finite temperature. In Fig. 12 uncertainty estimates derived from variations in the cutoff scale and nuclear contact terms are shown. For densities $\rho \gtrsim \rho_0$ the deviations increase, and are (surprisingly) larger between n3lo450 and n3lo414 as compared to n3lo500 and n3lo414. Figure 12 also shows the effect of varying the width of the DDNN regulator independently (with respect to the NN regulator). One sees that moderate variations have no large impact on the results. In particular, the effect is almost identical for different temperatures.

[7]These reduced isospin factors follow from the absence of proton lines in the Hartree and Fock diagrams in Fig. 2.

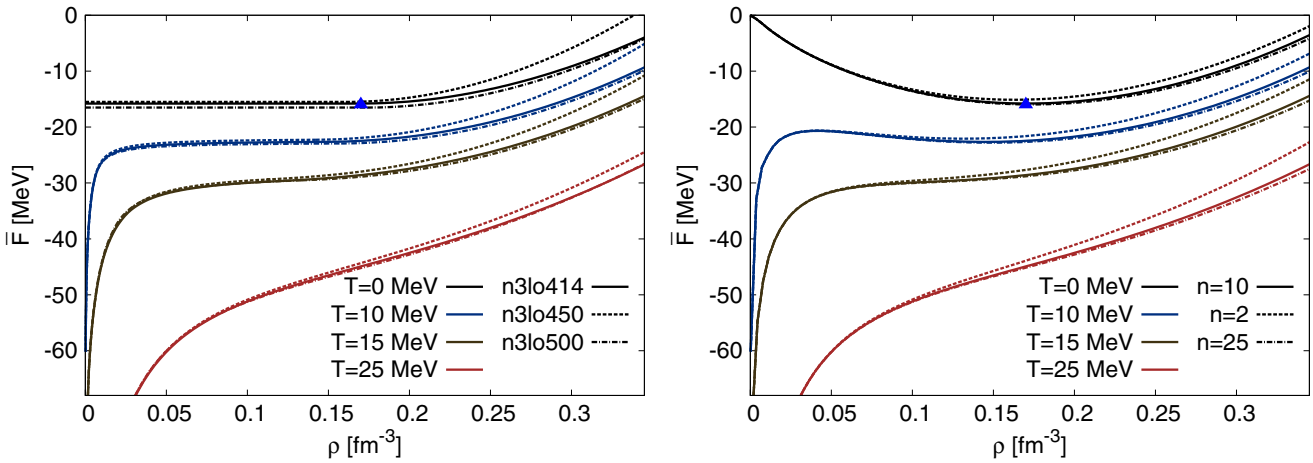

FIG. 12. (Color online) Uncertainty bands in the results for the free energy per nucleon $\bar{F}(\rho, T)$ resulting from the different n3lo potential sets, i.e., from differently regularized chiral interactions, and from independently varying the DDNN regulator. The curves in the second plot have been calculated using n3lo414 and show the results without the Maxwell construction applied. The blue triangle marks the empirical saturation point.

V. SUMMARY

We have calculated the thermodynamic equation of state of isospin-symmetric nuclear matter using nuclear potentials derived within the framework of chiral effective field theory. The dependence of nuclear matter properties on both the choice of the cutoff scale in the regulating function as well as the values of the low-energy constants associated with the N2LO chiral three-nucleon force were studied. Thermodynamically consistent results have been obtained with chiral nuclear potentials whose two-body low-energy constants have been fit to NN scattering phase shifts at the cutoff scales 414,450,and 500 MeV and whose three-nucleon contact terms were fit to the triton binding energy and lifetime. The results presented in this work (particularly for the critical temperature, critical density, and critical pressure) therefore represent genuine predictions of nuclear many-body dynamics with constraints coming only from nuclear few-body systems. In the cases considered, good reproduction of the zero-temperature saturation point and compressibility led to consistent thermodynamics, and in particular a narrow range for the critical temperature $T_c = 17.2$–19.1 MeV of the liquid-gas phase transition.

In future work we plan to extend our calculations to the case of isospin-asymmetric nuclear matter, with pure neutron matter as a limiting case. This will allow for the comparison of additional observables such as the symmetry energy and the isobaric compressibility. Such calculations will be key to constructing microscopic equations of state for use in numerically intense simulations of astrophysical phenomena. Additionally, from the quark-mass dependence of the chiral potentials it will be possible to determine the thermodynamic properties of the in-medium chiral condensate related to spontaneous symmetry breaking. Including the effects of subleading many-nucleon forces as well as explicit $\Delta(1232)$-isobar degrees of freedom represent future challenges.

ACKNOWLEDGMENTS

This work is supported in part by BMBF, by the DFG–NSFC (CRC 110), and U.S. DOE Grant No. DE-FG02-97ER-41014.

[1] P. Demorest, T. Pennucci, S. Ransom, M. Roberts, and J. Hessels, Nature (London) **467**, 1081 (2010).
[2] J. Antoniadis, P. C. C. Freire, N. Wex, T. M. Tauris, R. S. Lynch *et al.*, Science **340**, 6131 (2013).
[3] J. M. Lattimer, Ann. Rev. Nucl. Part. Sci. **62**, 485 (2012).
[4] T. Hell and W. Weise, arXiv:1402.4098.
[5] J. B. Elliott, P. T. Lake, L. G. Moretto, and L. Phair, Phys. Rev. C **87**, 054622 (2013).
[6] V. Karnaukhov, H. Oeschler, A. Budzanowski, S. Avdeyev, A. Botvina *et al.*, Phys. Atom. Nucl. **71**, 2067 (2008).
[7] N. Kaiser, S. Fritsch, and W. Weise, Nucl. Phys. A **697**, 255 (2002).
[8] K. Hebeler and A. Schwenk, Phys. Rev. C **82**, 014314 (2010).
[9] K. Hebeler, S. K. Bogner, R. J. Furnstahl, A. Nogga, and A. Schwenk, Phys. Rev. C **83**, 031301 (2011).
[10] I. Tews, T. Krüger, K. Hebeler, and A. Schwenk, Phys. Rev. Lett. **110**, 032504 (2013).
[11] J. W. Holt, N. Kaiser, and W. Weise, Phys. Rev. C **87**, 014338 (2013).
[12] L. Coraggio, J. W. Holt, N. Itaco, R. Machleidt, and F. Sammarruca, Phys. Rev. C **87**, 014322 (2013).
[13] T. Krüger, I. Tews, K. Hebeler, and A. Schwenk, Phys. Rev. C **88**, 025802 (2013).
[14] A. Carbone, A. Polls, and A. Rios, Phys. Rev. C **88**, 044302 (2013).
[15] A. Gezerlis, I. Tews, E. Epelbaum, S. Gandolfi, K. Hebeler, A. Nogga, and A. Schwenk, Phys. Rev. Lett. **111**, 032501 (2013).
[16] J. W. Holt, N. Kaiser, and W. Weise, Prog. Part. Nucl. Phys. **73**, 35 (2013).
[17] G. Hagen, T. Papenbrock, A. Ekström, K. A. Wendt, G. Baardsen, S. Gandolfi, M. Hjorth-Jensen, and C. J. Horowitz, Phys. Rev. C **89**, 014319 (2014).
[18] C. Drischler, V. Soma, and A. Schwenk, Phys. Rev. C **89**, 025806 (2014).
[19] L. Coraggio, J. W. Holt, N. Itaco, R. Machleidt, L. E. Marcucci, and F. Sammarruca, Phys. Rev. C **89**, 044321 (2014).
[20] A. Roggero, A. Mukherjee, and F. Pederiva, Phys. Rev. Lett. **112**, 221103 (2014).
[21] G. Wlazłowski, J. W. Holt, S. Moroz, A. Bulgac, and K. J. Roche, arXiv:1403.3753.
[22] L. Tolos, B. Friman, and A. Schwenk, Nucl. Phys. A **806**, 105 (2008).
[23] S. Fiorilla, N. Kaiser, and W. Weise, Nucl. Phys. A **880**, 65 (2012).
[24] G. Sauer, H. Chandra, and E. Mosel, Nucl. Phys. A **264**, 221 (1976).
[25] J. W. Holt, N. Kaiser, and W. Weise, Phys. Rev. C **79**, 054331 (2009).
[26] J. W. Holt, N. Kaiser, and W. Weise, Phys. Rev. C **81**, 024002 (2010).
[27] E. Epelbaum, H.-W. Hammer, and U.-G. Meissner, Rev. Mod. Phys. **81**, 1773 (2009).
[28] R. Machleidt and D. R. Entem, Phys. Rep. **503**, 1 (2011).
[29] P. Büttiker and U.-G. Meissner, Nucl. Phys. A **668**, 97 (2000).
[30] E. Epelbaum, A. Nogga, W. Glöckle, H. Kamada, U.-G. Meissner, and H. Witala, Eur. Phys. J. A **15**, 543 (2002).
[31] M. C. M. Rentmeester, R. G. E. Timmermans, and J. J. de Swart, Phys. Rev. C **67**, 044001 (2003).
[32] D. R. Entem and R. Machleidt, Phys. Rev. C **68**, 041001 (2003).
[33] L. Coraggio, A. Covello, A. Gargano, N. Itaco, D. R. Entem, T. T. S. Kuo, and R. Machleidt, Phys. Rev. C **75**, 024311 (2007).
[34] S. K. Bogner, R. J. Furnstahl, and A. Schwenk, Prog. Part. Nucl. Phys. **65**, 94 (2010).
[35] E. Marji, A. Canul, Q. MacPherson, R. Winzer, C. Zeoli, D. R. Entem, and R. Machleidt, Phys. Rev. C **88**, 054002 (2013).
[36] R. J. Furnstahl, Nucl. Phys. Proc. Suppl. **228**, 139 (2012).
[37] S. K. Bogner, T. T. S. Kuo, and A. Schwenk, Phys. Rep. **386**, 1 (2003).
[38] A. Nogga, S. K. Bogner, and A. Schwenk, Phys. Rev. C **70**, 061002 (2004).

[39] S. K. Bogner, A. Schwenk, R. J. Furnstahl, and A. Nogga, Nucl. Phys. A **763**, 59 (2005).
[40] S. Fritsch, N. Kaiser, and W. Weise, Phys. Lett. B **545**, 73 (2002).
[41] K. A. Brueckner and J. L. Gammel, Phys. Rev. **109**, 1023 (1958).
[42] J. Goldstone, Proc. R. Soc. Lond. A **239**, 267 (1957).
[43] R. K. P. Zia, E. F. Redish, and S. R. McKay, Am. J. Phys. **77**, 614 (2009).
[44] W. Kohn and J. M. Luttinger, Phys. Rev. **118**, 41 (1960).
[45] J. M. Luttinger and J. C. Ward, Phys. Rev. **118**, 1417 (1960).
[46] J. W. Holt, N. Kaiser, and W. Weise, Nucl. Phys. A **870-871**, 1 (2011).
[47] J. W. Holt, N. Kaiser, G. A. Miller, and W. Weise, Phys. Rev. C **88**, 024614 (2013).
[48] E. D. Jurgenson, P. Navratil, and R. J. Furnstahl, Phys. Rev. C **83**, 034301 (2011).
[49] K. Hebeler, Phys. Rev. C **85**, 021002 (2012).
[50] S. Typel, G. Röpke, T. Klahn, D. Blaschke, and H. H. Wolter, Phys. Rev. C **81**, 015803 (2010).
[51] D. Vretenar, T. Niksic, and P. Ring, Phys. Rev. C **68**, 024310 (2003).
[52] L.-W. Chen, B.-J. Cai, C. M. Ko, B.-A. Li, C. Shen, and J. Xu, Phys. Rev. C **80**, 014322 (2009).
[53] J. P. Blaizot, Phys. Rep. **64**, 171 (1980).
[54] N. Kaiser, Eur. Phys. Jour. A **48**, 135 (2012).